Effects of Liquid Phase Cloud Microphysical Processes in Mixed Phase Cumulus Clouds over the Tibetan Plateau

Xiaoqi Xu[1], Chunsong Lu[1*], Yangang Liu[2*], Wenhua Gao[3], Yuan Wang[1], Yueming Cheng[1], Shi Luo[1], Kwinten Van Weverberg[4]

1. Key Laboratory for Aerosol-Cloud-Precipitation of China Meteorological Administration/Collaborative Innovation Center on Forecast and Evaluation of Meteorological Disasters (CIC-FEMD), Nanjing University of Information Science & Technology, Nanjing, China

2. Environmental and Climate Sciences Department, Brookhaven National Laboratory, Upton, US

3. State Key Laboratory of Severe Weather, Chinese Academy of Meteorological Sciences, Beijing, China

4. Met Office, Exeter, UK

* Correspondence: luchunsong110@gmail.com; lyg@bnl.gov

Key points:

1. The accretion process plays more important roles than other examined liquid-phase processes.
2. Considering raindrop size in accretion process suppresses liquid-phase rain and mitigates the overprediction of precipitation over the TP.
3. Increasing the model resolution can reduce precipitation overprediction.

Abstract

Numerical simulations often overpredict precipitation over the Tibetan Plateau. To examine the factors causing precipitation overprediction, a typical summer plateau precipitation event is simulated with the Weather Research and Forecasting (WRF) model by exploring different parameterizations of liquid-phase microphysical processes into the commonly used Morrison scheme, including autoconversion, accretion, and entrainment-mixing. All simulations can reproduce the general spatial distribution and temporal variation of precipitation, but overpredict precipitation rate. The results show that the accretion process is more important than other examined liquid-phase processes in simulating precipitation. Further investigation reveals that accretion parameterization that takes into account the raindrop size produces the most accurate results in terms of the total surface precipitation, which is supported by the Heidke skill scores. Such parameterizations suppress spurious accretion and liquid-phase precipitation when cloud droplets are too small to initiate precipitation. It is also confirmed that increasing the model resolution can reduce precipitation overprediction. Results from the case study are confirmed by use of a one-month simulation.

1. Introduction

The Tibetan Plateau (TP) is the highest and largest plateau of the world with an average elevation of more than 4 km above the sea level and an area larger than 2.5 × 10^6 km^2. Its active exchanges of heat and moisture have significant influences on climate and environmental change, not only in China but also over East Asia and even the entire northern hemisphere through strong thermal and dynamic forcing (*Yeh*, 1950; *Flohn*, 1957; *Hahn and Manabe*, 1975; *Ye*, 1981; *Wu and Chen*, 1985; *Yanai et al.*, 1992; *Ding et al.*, 2001; *Wang et al.*, 2008; *Molnar et al.*, 2010; *Yang et al.*, 2014; *Qie et al.*, 2005; *Fu et al.*, 2006; *Li and Zhang*, 2017; *Li et al.*, 2020). Many studies have reported that the tropospheric heating over the TP has decisive effects on the maintenance of the Asian summer monsoon (*Luo and Yanai*, 1983; 1984; *Ueda and Yasunari*, 1998). The upward transport of sensible heat and the release of latent heat due to convective clouds are important heat sources in the upper troposphere, driving the summer monsoon and associated precipitation (*Nitta*, 1983; *Luo and Yanai*, 1984; *Yanai and Li*, 1994; *Ueda et al.*, 2003; *Hsu and Liu*, 2003; *Fan et al.*, 2013; *Jiang et al.*, 2004; *Li et al.*, 2013).

During the summer monsoon, deep convection develops over the TP with a marked diurnal cycle in precipitation (*Fujinami and Yasunari*, 2001; *Kurosaki and Kimura*, 2002; *Chen et al.*, 2017a), frequently associated with mesoscale vortices (*Shen et al.*, 1986; *Wang et al.*, 1993; *Li et al.*, 2008b). Summer precipitation on the plateau can be characterized by frequent, but rather weak convection (*Li et al.*, 2008b; *Li and Zhang*, 2016; *Gao et al.*, 2016; *Chen et al.*, 2017a). Undoubtedly, these characteristics are

heavily influenced by the unique terrain of the TP (*Porcù et al.*, 2014; *Chen et al.*, 2017b; *Wu and Liu*, 2017).

The particularity of the TP makes it one of the most challenging areas for precipitation simulation. Many studies find simulated precipitation to be overpredicted (*Maussion et al.*, 2011; *Xu et al.*, 2012; *Gao et al.*, 2016). There are several reasons for this overprediction, including model resolution (*Sato et al.*, 2008, *Xu et al.*, 2012) and the initial and boundary conditions (*Gerken et al.*, 2013). Moreover, the assumptions in the parameterization of microphysics could be another culprit for the overprediction of precipitation over the TP region. *Maussion et al.* (2011) found a significant sensitivity to changing the microphysics parameterization for convective precipitation over the TP. They compared different physical schemes with different statistical evaluation scores and the results showed that the effects of microphysics schemes were larger than other physical schemes including cumulus schemes, land surface schemes, and boundary-layer schemes.

The high elevation of the TP, and hence the typically low melting level, enables plenty of supercooled liquid water, even in summer (*Gao et al.*, 2016; *Zhao et al.*, 2017; *Tang et al.*, 2019). Therefore, it is likely that liquid precipitation processes play a role in the precipitation overestimation in this region. For instance, *Zhao et al.* (2017) confirmed that supercooled cloud water dominated in precipitating cumulus clouds over the Naqu area at a temperature of -2.5 to -3.5°C. By analyzing the raindrop size distribution at Maqu over the TP, *Li et al.* (2006) argued that liquid-phase processes

were important for surface precipitation, despite dominant ice/mixed-phase rain processes over the region. *Gao et al.* (2016) investigated the role of liquid-phase processes by excluding ice-phase microphysics, doubling the condensation rate, halving the evaporation rate and increasing the initial droplet radius, and found significant effects from all these sensitivity tests on the surface precipitation; they also suggested that liquid-phase rain processes could be more important than ice-phase processes over the precipitation cores during weak convection over the TP.

However, it is still unknown how liquid-phase processes affect precipitation over the TP, and whether improving the parameterizations of liquid-phase processes can mitigate the problem of overpredicted precipitation. Also unknown is which liquid-phase process is the most important in affecting TP precipitation, and which parameterization can best describe the most important process and why. This study fills these gaps by comparing simulations of a typical precipitation event over the TP with different parameterizations of autoconversion, accretion, and entrainment-mixing processes (hereafter referred to as liquid-phase processes for convenience) and dissecting the underlying physical mechanisms. This is done using a case study, as well as a one-month simulation. Moreover, the impact of model resolution is investigated following *Sato et al.* (2008) and *Xu et al.* (2012).

Three parameterized liquid-phase processes related to precipitation are investigated in this paper: autoconversion, accretion, and entrainment-mixing. These three processes are likely to be intertwined. It is expected that accretion and ice/mixed-

103 phase processes matter in the precipitation events over TP. But also, autoconversion and
104 entrainment-mixing process may be important. The reason is that accretion is the
105 collection process between liquid raindrops and cloud droplets, and the number
106 concentration and size of liquid droplets are affected by autoconversion and
107 entrainment-mixing process. Autoconversion is expressed as the mass conversion rate
108 from cloud to rain due to the collision-coalescence of cloud droplets while accretion is
109 defined as the rate of mass conversion from cloud to rain due to the collection of cloud
110 droplets by raindrops (*Wood et al.*, 2009; *White et al.*, 2017; *Liu and Daum*, 2004; *Liu*
111 *et al.*, 2011; *Jing et al.*, 2019; *Fan et al.*, 2016; *Wang et al.*, 2019b). The sum of
112 autoconversion and accretion is calculated as the total mass conversion from cloud to
113 raindrop populations during the collision-coalescence process (*Wood*, 2005b). *Wang et*
114 *al.* (2012) and *Gettelman et al.* (2013) highlighted that autoconversion was important
115 for the initiation of precipitation whereas accretion was responsible for the amount of
116 precipitation. The process of entrainment and mixing between cloud and environment
117 is one of the most uncertain processes in cloud physics (*Kollias and Albrecht*, 2000;
118 *Grabowski*, 2006; Lu et al., 2013; *Hoffmann and Feingold*, 2019; *Gao et al.*, 2020). The
119 key issue of the entrainment-mixing process is whether evaporation due to mixing
120 causes a reduction of only droplet size (homogeneous mixing), only droplet number
121 (extremely inhomogeneous mixing), or both. Therefore, different entrainment-mixing
122 mechanisms can affect cloud microphysical properties and hence cloud-related
123 processes such as radiation and precipitation (*Lasher-Trapp et al.*, 2005; *Grabowski*,

2006; *Chosson et al.*, 2007; *Slawinska et al.*, 2008; *Cooper et al.*, 2013; *Lu et al.*, 2013).

This paper is organized as follows: A brief introduction of the precipitation event and experimental setup are given in section 2. Section 3 discusses the influences of liquid-phase processes on precipitation overprediction and underlying physical mechanisms. Section 4 extends the case study to one-month simulations. The effects of resolutions on precipitation overprediction are discussed in section 5. Section 6 presents the summary and conclusions.

2. Precipitation event, experiment description, and method

2.1 Case description and observations

As mentioned in *Gao et al.* (2016), the entire plateau experienced a large frontal system from 21 to 23 July 2014 and observed precipitation initiated at 0400 UTC (Coordinated Universal Time) 22 July. The motivation of using this case is that WRF can capture the main precipitation pattern (Gao et al., 2016). Gao et al. (2016) and this study focus on different periods and different scientific questions. As mentioned in the introduction, Gao et al. (2016) studieded the sensitivity of precipitation to doubling droplet concentration, halving raindrop evaporation, and increasing initial cloud droplet size. This study focuses on different parameterizations of autoconversion, accretion, and entrainment-mixing. The simulations are compared against the precipitation dataset that *Ma et al.* (2018) derived from sparse gauge observations and multiple satellite precipitation datasets, including Tropical Rainfall Measuring Mission (TRMM)

Multisatellite Precipitation Analysis (TMPA) 3B42RT and 3B42V7 (*Huffman et al.*, 2007), Climate Prediction Center MORPHing technique (CMORPH) (*Joyce et al.*, 2004) and Precipitation Estimation from Remotely Sensed Information using Artificial Neural Networks-Climate Data Record (PERSIANN-CDR) (*Ashouri et al.*, 2015). This rain gauge dataset developed by *Ma et al.* (2018) is more accurate than individual gauges for complex terrains such as the TP region. This dataset also has higher spatial (0.1°) and temporal (1 h) resolution than TRMM, which is usually used in this region (*Fu et al.*, 2007; *Yin et al.*, 2008; *Maussion et al.*, 2011; *Xu et al.*, 2012; *Qie et al.*, 2014).

2.2 Model and experiment description

The WRF model version 3.8.1 is used to simulate this typical summer TP precipitation event. The WRF model is a next-generation mesoscale numerical weather prediction system designed for both atmospheric research and operational forecasting applications. Here, WRF is used as a cloud-resolving model with 1 km horizontal grid spacing for the innermost domain (referred to as domain 03) with 276×276×45 grid points, which covers most of the plateau center; the spatial resolutions for the two outer domains (01 and 02) are 25 km and 5 km with 200×200×45 and 176×176×45 grid points, respectively (Figure 1). Initial and boundary conditions are provided by the National Center for Environmental Prediction Final operational global analysis data with 1° spatial and 6 h temporal resolution. The simulation starts at 1200 UTC 21 July and ends at 0000 UTC 24 July, with a total of 60 h integration time. We focus on the

results of the last 48 h from domain 02 and domain 03 with a 30-minute interval.

The microphysics scheme used in the control run is the Morrison double-moment scheme (*Morrison and Grabowski*, 2008). Note that this bulk scheme is different from the default version released in the WRF model with a fixed cloud droplet number concentration (N_c) (e.g. N_c = 250 cm^{-3}). This version can predict the number concentration and mass mixing ratios of cloud droplets (N_c, q_c), raindrops (N_r, q_r), ice crystals (N_i, q_i), snow particles (N_s, q_s), and graupel particles (N_g, q_g) followed *Morrison et al.* (2005). The main liquid-phase conversion processes, i.e. autoconversion rate (A_u; kg/kg/s) and accretion rate (A_c; kg/kg/s), are both based on *Khairoutdinov and Kogan* (2000), further referred to as the KK00 schemes:

$$A_u = 1350 \times q_c^{2.47}(N_c \times 10^{-6} \times \rho_a)^{-1.79}, \quad (1)$$

$$A_c = 67 \times (q_c q_r)^{1.15}, \quad (2)$$

where ρ_a is the air density.

To explore the influence of liquid-phase cloud microphysical processes in mixed-phase clouds, we implement several different expressions for autoconversion, accretion, and entrainment-mixing into the Morrison scheme, and examine the model sensitivity. In addition to the default KK00 schemes, three commonly-used autoconversion schemes are employed and referred to as Be68, Bh94, and LD04 for convenience, respectively:

1) Be68:

$$A_u = \frac{3.5\times10^{-2} q_c^2}{0.12+1.0\times10^{-12}\frac{N_c}{q_c}}, \quad (3)$$

This is the default scheme in several global climate models, such as Model for Interdisciplinary Research on Climate version 5 (MIROC5; *Michibata and Takemura*, 2015; *Jing and Suzuki*, 2018).

2) Bh94:

$$A_{\mathrm{u}} = 6.0 \times 10^{28} n^{-1.7} (q_{\mathrm{c}} \times 10^{-3})^{4.7} (N_{\mathrm{c}} \times 10^{-6})^{-3.3}, \quad (4)$$

where n is set to 10 in Eq. 4, which is related to the width of cloud droplet size distribution (*Beheng*, 1994).

3) LD04:

$$A_{\mathrm{u}} = P_0 T\,, \quad (5a)$$

$$P_0 = 1.1 \times 10^{13} \left[\frac{(1+3\varepsilon^2)(1+4\varepsilon^2)(1+5\varepsilon^2)}{(1+\varepsilon^2)(1+2\varepsilon^2)} \frac{q_{\mathrm{c}}^3}{N_{\mathrm{c}}}\right], \quad (5b)$$

$$T = \frac{1}{2}(x_{\mathrm{c}}^2 + 2x_{\mathrm{c}} + 2)(1 + x_{\mathrm{c}}) e^{-2x_{\mathrm{c}}}, \quad (5c)$$

$$x_{\mathrm{c}} = 9.7 \times 10^{-14} N_{\mathrm{c}}^{3/2} q_{\mathrm{c}}^{-2}. \quad (5d)$$

LD04 derived by *Liu and Daum* (2004) and *Liu* (2005) considers relative dispersion ε (the ratio of the standard deviation to the mean radius) in addition to droplet concentration and liquid water mixing ratio. This scheme was implemented into the WRF double-moment schemes (*Xie and Liu*, 2011; *Xie et al.*, 2013). P_0 and T represent the rate function and threshold function, respectively; x_{c} is the normalized critical mass and can be written as a function of N_{c} and q_{c} (Liu et al., 2005); ε is set to 0.4 as the average value based on *Zhao et al.* (2006) and *Wang et al.* (2019a).

Considering that most accretion schemes only consider mass mixing ratios of cloud droplets and raindrops (i.e. q_{c} and q_{r}) (e.g. *Beheng*, 1994; *Khairoutdinov and*

208 *Kogan*, 2000; *Kogan*, 2013), a parameterization that relates the accretion process to
209 liquid droplet number concentration and size is adopted from *Cohard and Pinty* (2000),
210 named as CP2k:

211 $$A_{\mathrm{c}} = \frac{\pi}{6}\rho_{\mathrm{W}}\rho_{\mathrm{a}}K_1\frac{N_{\mathrm{c}}N_{\mathrm{r}}}{\lambda_{\mathrm{c}}^3}\left(\frac{A_1}{\lambda_{\mathrm{c}}^3}+\frac{B_1}{\lambda_{\mathrm{r}}^3}\right),$$

212 $$if\ R_{\mathrm{r}} \geq 50\ \mu m, \text{and} \tag{6a}$$

213 $$A_{\mathrm{c}} = \frac{\pi}{6}\rho_{\mathrm{W}}\rho_{\mathrm{a}}K_2\frac{N_{\mathrm{c}}N_{\mathrm{r}}}{\lambda_{\mathrm{c}}^3}\left(\frac{A_2}{\lambda_{\mathrm{c}}^6}+\frac{B_2}{\lambda_{\mathrm{r}}^6}\right),$$

214 $$if\ R_{\mathrm{r}} < 50\ \mu m, \tag{6b}$$

215 where ρ_{W} is the water density; R_{r} is the raindrop radius; K_1 and K_2 are empirical
216 constants; the subscripts *c* and *r* denote cloud droplets and raindrops, respectively; A_1,
217 A_2, B_1, and B_2 are functions related to the two dispersion parameters of the modified
218 Gamma size distribution (*Cohard and Pinty*, 2000) and their expressions are given in
219 Appendex B; λ is the slope parameter and is derived from the dispersion parameter,
220 number concentration and mixing ratio of the species (see *Morrison et al.*, 2005). Given
221 the specified dispersion parameters for raindrops, $\lambda_{\mathrm{r}} = (\pi\rho_{\mathrm{W}}N_{\mathrm{r}}/q_{\mathrm{r}})^{1/3}$ which is
222 inversely proportional to the mean volume radius of the raindrops. Another accretion
223 scheme (Ko13, *Kogan*, 2013) is also tested:

224 $$A_{\mathrm{c}} = 8.53 \times q_c^{1.05}{q_r}^{0.98}, \tag{7}$$

225 A single parameter α is used to represent the effect of entrainment-mixing process
226 in this microphysical scheme (*Morrison and Grabowski*, 2008; *Lu et al.*, 2013):

227 $$N_c = N_{\mathrm{c0}}\left(\frac{q_{\mathrm{c}}}{q_{\mathrm{c0}}}\right)^{\alpha}, \tag{8}$$

228 where the N_{c} and N_{c0} are the number concentrations of cloud water droplets after and

229 before the evaporation process, respectively; q_c and q_{c0} represent the corresponding
230 mixing ratios, respectively. It is noteworthy that q_c is mainly determined by q_{c0}, relative
231 humidity, air pressure, and temperature when new saturation is achieved after
232 evaporation. The parameter α can be set to any value between 0 and 1 corresponding to
233 a different degree of the subgrid-scale mixing homogeneity. When α = 0, homogeneous
234 mixing is assumed (the control run). On the contrary, when α = 1, extremely
235 inhomogeneous mixing is assumed (the INHOMO run).

236 In total, we have 7 simulations: the control run with the KK00 schemes for
237 autoconversion and accretion, and homogeneous mixing, and sensitivity tests with three
238 autoconversion schemes (Be68, Bh94, and LD04), two accretion schemes (CP2k and
239 Ko13), and one entrainment-mixing scheme (INHOMO). The case names and
240 corresponding formulations are summarized in Table 1.

241

242 **2.3 Calculations of microphysical/radiative properties**

243 The liquid cloud water path (LCWP) is calculated by

244 $$\mathrm{LCWP} = \int_0^H \rho_a q_c(z) dz, \quad (9)$$

245 where $q_c(z)$ is the cloud water mixing ratio at each height (z). The equation for cloud
246 optical depth (τ) is:

247 $$\tau = \frac{3}{2}\frac{1}{\rho_w}\int_0^H \frac{\rho_a q_c(z)}{r_e(z)} dz, \quad (10)$$

248 where $r_e(z)$ is the effective radius of cloud droplets at each height (z); the extinction
249 efficiency is assumed to equal to 2 (appropriate at visible wavelengths) (*Grabowski*,

2006); H is the cloud top height. With equations (9) and (10), the column mean effective radius ($\overline{r_e}$) is given by

$$\overline{r_e} = \frac{3}{2}\frac{LCWP}{\rho_w \tau}, \quad (11)$$

Note that only the cloud data in the grid boxes with hydrometeor mixing ratios larger than 0.01 g/kg are included.

3. Case study Analysis

3.1 Control run

3.1.1 Precipitation from the control run and observations

The 48 h accumulated precipitation from 0000 UTC 22 July to 0000 UTC 24 July 2014 from the control run over domain 02 and domain 03 are averaged to the resolution of 0.1° to compare with observations (Figure 2). The results from domain 02 indicate that the control run can reproduce the primary rainband. The observed precipitation in most regions is less than 50 mm and the maximum value is approximately 80 mm. Although the control run is spatially consistent with the observations, the maximum simulated precipitation is about 200 mm, largely exceeding the observed value. Similar biases were reported in *Xu et al.* (2012) and *Gao et al.* (2016). For domain 03, when the simulated precipitation is averaged to 0.1°, there are only about 27x27 data points; this data volume is insufficient to compare the spatial distribution of precipitation between simulations and observations. This could explain the spatial precipitation bias shown in Figures 2c and 2d. Besides spatial comparison, Figures 3a and 3b show the

271 temporal evolutions of area-averaged hourly precipitation rate from the observation and
272 the control run over domain 02 and domain 03, respectively. The black solid lines
273 denote the observations. The simulations of both domains temporally correlate well
274 with observations, but the domain 03 is clearly closer to the observations in terms of
275 precipitation rate. The observations for domain 03 show that there are two peaks of
276 precipitation in the local afternoon (UTC + 6 h). The first precipitation event starts from
277 0400 UTC and ends at 1800 UTC with the maximum precipitation rate of 1.0 mm/h
278 attained at 0900 UTC. The other precipitation peak is weak with a maximum
279 precipitation rate of only about 0.4 mm/h. The time of the peaks in the simulations is
280 about 2 hours later than that in the observations, which was also reported in *Gao et al.*
281 (2018).

282 Generally speaking, the control run captures the main features of the precipitation
283 evolution (the peaks and the trends). However, compared with the observations of 48 h
284 accumulated precipitation over the corresponding areas, the control run overpredicts
285 precipitation by 51.5% in domain 02 and by 20.8% in domain 03.

286

287 **3.1.2 Microphysical processes in the control run**

288 To examine the origin of the precipitation biases discussed above, a more in-depth
289 analysis of the microphysics is performed for both domains 02 and 03. For domain 02,
290 considering that the altitude of the southeastern corner is lower than the other regions,
291 liquid-phase precipitation is expected to be stronger. Therefore, domain 02 is divided

292 into two parts: the southeastern corner and the other regions. For domain 03, the two
293 precipitation peak periods are studied separately.

294 Figure 4 shows the mean vertical profiles of five types of hydrometeors and their
295 primary microphysical processes for the two separate regions over domain 02 and the
296 two precipitation peaks (5 hours) over domain 03, respectively. For domain 02, mixing
297 ratios of ice-phase hydrometeors (ice, snow, and graupel) and rates of microphysical
298 processes (RIM-s, RIM-g, MELT) over the southeastern corner (Figures 4c and d) are
299 generally equivalent to or smaller than those over the other regions (Figures 4a and b).
300 Mixing ratios of liquid-phase hydrometeors (cloud and rain) and microphysical
301 processes (ACCR-r, AUTO-r) are larger over the southeastern corner than those over
302 the other regions. As mentioned above, liquid droplets will grow more favorably over
303 the southeastern corner because of its lower terrain. For domain 03, mixing ratios of
304 ice-phase hydrometeors (ice, snow, and graupel) and rates of microphysical processes
305 (EVAP-r, ACCR-s, RIM-s, RIM-g, MELT) are smaller during the second peak period
306 (Figures 4g and h) than those during the first peak (Figures 4e and f). On the other hand,
307 accretion of cloud droplets by rain (ACCR-r) is larger for the second peak than for the
308 first one, while melting still dominates. By calculating the vertical accumulated
309 conversions of liquid-phase processes (ACCR-r and AUTO-r) and ice-phase processes
310 to raindrops, the contributions of ACCR-r and AUTO-r are 32.86%, 65.20%, 27.03%,
311 and 35.41% for other regions in domain 02 except southeastern corner, the southeastern
312 corner in domain 02, and two precipitation peaks in domain 03, respectively. Therefore,

313 the liquid-phase processes over the southeastern corner in domain 02 and the second
314 precipitation peak in domain 03 are more important than those over the other regions
315 in domain 02 and the first precipitation peak in domain 03, respectively. However, this
316 happens for different reasons. While ice phase processes are equally important across
317 the entire domain 02, the higher temperature in the lower southeastern corner allows
318 for more liquid-phase precipitation. In domain 03, however, the second peak is clearly
319 associated with smaller ice-related conversion rates.
320
321 **3.2 Sensitivity of precipitation overprediction to different liquid-phase processes**
322 Precipitation, microphysical properties, and their related processes from the
323 sensitivity simulations are discussed in this section, including Be68, Bh94, LD04, CP2k,
324 Ko13, and INHOMO. The effects of these schemes on precipitation overprediction are
325 examined in detail.
326
327 **3.2.1 Evaluation of surface precipitation**
328 The results for precipitation from the sensitivity tests are shown in Figures 5 and
329 6. All sensitivity tests reproduce a similar location, trend, and precipitation rate,
330 compared to the control run, except the CP2k experiment. CP2k has distinctly weaker
331 precipitation than the other simulations especially over the southeastern corner in
332 domain 02 and during the second precipitation peak period in domain 03. CP2k
333 overestimates precipitation by 30.2% in domain 02, which is an improvement compared

334 to the control and other sensitivity tests (48.8%-52.5%); in domain 03, the
335 overprediction in the CP2k is only 10.9%, also much smaller than the 15.1% in
336 INHOMO and 20.8%-26.9% in the control and other sensitivity tests. Some previous
337 studies found large variation of precipitation by using different autoconversion schemes
338 (*Li et al.*, 2008a; *Wang et al.*, 2013), while other studies showed that surface
339 precipitation was insensitive to the choice of autoconversion schemes (*Morrison and*
340 *Grabowski*, 2007; *Michibata and Takemura*, 2015). It seems that such a sensitivity may
341 vary by cloud regimes and even case by case. The limited effects of different
342 autoconversion schemes on the surface precipitation rate in this study could be related
343 to the dominance of melting and accretion in raindrop formation, and large precipitation
344 amount

345 The Heidke skill score (HSS) is used to further quantitatively evaluate the
346 simulations with different schemes:

347 $$\mathrm{HHS} = \frac{2(ad - bc)}{(a + c)(c + d) + (a + b)(b + d)}, \quad (12)$$

348 where the four elements *a*-*d* for HSS, representing the numbers of "hits", "false alarms",
349 "misses" and "correct negatives", respectively, are calculated from a contingency table
350 (Table 2). HHS can not only judge well-simulated events (both hits and correct
351 negatives, element *a* and *d*) but also account for the erroneous forecast (*b* and *c*)
352 (*Barnston*, 1992). A higher HSS (0-1) represents better skill. As shown in Table 2, p_t is
353 the threshold value and is set to be 2 mm covering most of the observed and simulated
354 precipitation area, p_s and p_o are the values from simulations and observations,

355 respectively.

356 The elements *a*-*d* and HSS for all sensitivity tests over domains 02 and 03 are
357 shown in Table 3. All the cases in domain 02 have the HSS scores exceeding 0.4 and
358 are close to each other except for CP2k. The impacts of changing autoconversion
359 schemes and mixing mechanisms on HSS are limited. The CP2k accretion scheme,
360 however, has significantly higher HSS than other cases, particularly due to its high
361 value of *d*, the "correct negatives" mainly over the southeastern region for domain 02.
362 The high HSS scores in CP2k indicate that changing the accretion scheme is a possible
363 way to improve the much-overestimated precipitation in simulations over this region.
364 The HSS scores of all simulations for domain 03 are small because there are too few
365 data points for evaluation, as mentioned above; slight changes in any of the four factors
366 can cause a large difference in the final scores. However, the CP2k case still has the
367 highest HSS of 0.152, much larger than the maximum and mean HSS of other cases,
368 0.110 and 0.076, respectively.

369

370 **3.2.2 Impact of liquid-phase parameterization on cloud properties**

371 Table 4 summarizes the microphysical properties for all the simulations, including
372 LCWP, $\overline{r_e}$ and N_c over domains 02 and 03, respectively. It is noteworthy that the CP2k
373 scheme has the largest effect on LCWP and $\overline{r_e}$ among all the sensitivity tests.
374 Compared to the control run, differences of the CP2k case over domain 02 (03) are
375 +64.6% (+51.0%) in LCWP and +7.9% (+5.6%) in $\overline{r_e}$ while the other accretion

376 sensitivity test, using Ko13, is much closer to the control run. The reasons will be
377 analyzed in Section 3.3.2. Cloud observational data from Clouds and the Earth's
378 Radiant Energy System (CERES) project with 1 h time resolution and 1° spatial
379 resolution are also provided in Table 4. Among all the simulations, the CP2k case has
380 the results of LCWP and $\overline{r_e}$ closest to the observations.

381 The difference between all autoconversion sensitivity tests and the control run for
382 LCWP and $\overline{r_e}$ are, respectively, from -13.7% to 10.6% and -1.9% to 2.3% over domain
383 02, and from -11.1% to 13.9% and -1.2% to 3.5% over domain 03. The wide ranges are
384 mainly caused by one order of magnitude difference of A_u amongst the different
385 sensitivity tests (Figures 7a and b). However, the magnitude of the difference is much
386 smaller than that in typical marine boundary layer clouds (*Wood*, 2005b), because of
387 the thinner liquid-phase layer and the involvement of ice/mixed-phase processes over
388 the TP. The sign of the difference between the schemes is consistent with previous
389 studies, e.g., Be68 and LD04 have larger A_u than KK00 (Figures 7a and b) (*Lee and*
390 *Baik*, 2017).

391 For the entrainment-mixing process, the INHOMO experiment has the largest
392 effect on N_c among all the sensitivity tests. Even so, there is only a modest reduction of
393 only 2.6 (4.9) /cm^3 compared to the control run, resulting in 0.9% (1.5%) larger $\overline{r_e}$ over
394 domain 02 (03). It seems that the influence of INHOMO in domain 03 is greater than
395 that in domain 02 since the relevant scales involved in the entrainment-mixing process
396 are usually small and domain 03 has a higher resolution than domain 02. Such a

variation of $\overline{r_e}$ over domain 03 is comparable with that in all the autoconversion schemes and Ko13. The variation of LCWP is smaller than that in the liquid conversion process. Sensitivity tests of all autoconversion and accretion schemes in Table 4 are also conducted assuming different mixing mechanisms (See supplement for details). The effects are also small, similar to several previous studies using double-moment microphysics schemes (*Hill et al.*, 2009; *Grabowski and Morrison*, 2011; *Slawinska et al.*, 2012). One important reason is that the relative humidity in entrained air is high (*Slawinska et al.*, 2012; *Hoffmann and Feingold*, 2019).

3.3 Reasons for improvements of precipitation overprediction in CP2k

As mentioned before, CP2k reduces the precipitation overprediction more significantly than other sensitivity tests. The reasons are discussed in this section.

3.3.1 Detailed microphysical processes in CP2k

CP2k experiences an A_c rate that is one to two orders of magnitude smaller than in the control run and other sensitivity tests (Figures 7c and d). The reason for why A_c in the control run and other sensitivity tests is so close is that the KK00 and the Ko13 schemes have similar functions of rain and cloud water content (Eqs. 2 and 7) and similar variation trends in Figure 9 (which is analyzed in Section 3.3.2 in detail). In each case, larger A_u enhances A_c by providing more rain drops. Therefore, the trend of A_c corresponds well to that of A_u. The result between different cases is different

418 from that in each case. Compared with the control run, A_c in CP2k is smaller, and thus
419 fewer cloud droplets are collected by raindrops; these surviving cloud droplets are then
420 available for autoconversion, which leads to the larger A_u in CP2k (e.g. *Gettelman et*
421 *al.*, 2013; *Posselt and Lohmann*, 2008). As shown in Figures 7a and b, A_u in CP2k is
422 much larger than that in the control run; the difference is close to the value from
423 applying different autoconversion schemes. Therefore, CP2k has the lowest ratio
424 A_c/A_u with the mean value of 2.88 (2.81) over domain 02 (03) mainly because of small
425 A_c. Bh94 has the largest ratio A_c/A_u with a mean value of 151.24 (144.60) over
426 domain 02 (03). Indeed, Bh94 exhibits the smallest A_u (Figures 7e and f) of all
427 schemes tested here. A_c/A_u of all schemes is in the range of 0.1-296.3, consistent with
428 previous studies (*Gettelman et al.*, 2013; *Lee and Baik*, 2017; *Michibata and Takemura*,
429 2015; *Seifert and Onishi*, 2016; *Jiang et al.*, 2010). In domain 03, A_c/A_u larger than 1
430 usually corresponds to larger precipitation intensity; A_c/A_u smaller than 1 usually
431 corresponds to smaller precipitation at the start or the end of precipitation events. This
432 correspondence is consistent with the arguments as to accretion-dominated and
433 autoconversion-dominated regimes (*Jiang et al.*, 2010; *Wood et al.*, 2009; *Michibata*
434 *and Takemura*, 2015). In domain 02, most of A_c/A_u is larger than 1; some A_c/A_u
435 values are smaller than 1 but still with strong precipitation likely caused by the
436 influence of ice/mixed-phase processes.

437 Combining two dominant liquid-phase rain formation processes (autoconversion
438 and accretion), less cloud water is depleted in CP2k; as a result, the mean value of

LCWP is over 50.0% larger than that of the control run, as shown in Table 4. Figure 8 shows the vertical profiles of the mean differences of the dominant conversion process rates between CP2k and the control run (CP2k-Control) over the two regions in domain 02 and during the two precipitation peak periods in domain 03. Similar to Figure 7, CP2k has a much smaller A_{c} and larger A_{u}. Despite the larger A_{u}, many cloud droplets are suspended above the 0 ℃ isotherm, beneficial for riming of cloud droplets onto snow or graupel particles (RIM-s + RIM-g). Figure S1 in the supplementary material shows the microphysical processes conversion rates in CP2k with riming minus those without riming. Riming suppresses the liquid-phase rain formation processes through reducing A_{c}, but enhances ice/mixed-phase rain formation processes through increasing melting rate. The sensitivity of warm/cold rain formation to riming ultimately trickles down to uncertainties in the simulation of surface precipitation.

Note that the smaller melting rate near 6 - 6.5 km in CP2k over domain 03 is because of the lower melting level in CP2k than in the control run. Given the larger water content, CP2k also has a larger optical depth τ (14.3) than the control run (11.1), which means more solar radiation is reflected to the upper atmosphere and less short-wave radiation reaches the ground (219.6 W/m^2 in CP2k vs 226.5 W/m^2 in the control run). Qualitatively, such a difference in radiation could be one reason responsible for a lower temperature in CP2k in the low atmosphere than in the control run, other things being equal (e.g., latent heating release). Therefore, the melting level is lower in CP2k.

The source of surface precipitation includes both the liquid-phase (mainly ACCR-

460 r) and the ice/mixed-phase. During the first precipitation peak period in domain 03,
461 despite the smaller A_c in CP2k than that in the control run, more riming leads to more
462 melting. The combination of weaker accretion and stronger melting in CP2k offset each
463 other, and hence the precipitation from CP2k and the control run is very close in this
464 period (Figure 6b). A similar chain of events also occurs in domain 02 except for the
465 southeastern corner (Figures 2b and 5d). However, in the control run, due to relatively
466 low concentration of ice particles during the second peak period in domain 03, the
467 liquid-phase processes, in particular accretion, become relatively more important
468 (Figure 4h); for the southeastern corner of domain 02, the large mixing ratio of cloud
469 droplets even causes A_c to exceed the melting rate (Figure 4d). Surface precipitation
470 is overestimated in the control run compared with the observations, as discussed in
471 Section 3.2.1. In CP2k, the accretion is suppressed which appears to alleviate the
472 overestimation of precipitation. Therefore, the total surface precipitation in CP2k is
473 smaller than that in the control run over the southeastern corner in domain 02 and during
474 the second peak period in domain 03, which is closer to observations.
475
476 **3.3.2 Theoretical analysis of the CP2k parameterization**
477 The large differences in cloud microphysics and precipitation between CP2k and
478 other cases can be explained based on the different equations for autoconversion and
479 accretion (Eqs. 2, 6 and 7). The different equations for the autoconversion and accretion
480 can be separated into two basic methods as mentioned in *Wood* (2005b): the first one

integrates the stochastic collection equation for a wide range of drop size distributions and then uses a simple power-law fit, such as the KK00 scheme in the control run. The second method simplifies the collection kernel and parameterizes the autoconversion and accretion processes, such as the parametrization of the A_{u} in LD04 and A_{c} in CP2k. Autoconversion schemes commonly use one of these basic methods. However, the accretion schemes used in most of the microphysical schemes are based on the first method, and previous studies focus on comparing accretion schemes using this method (*Wood*, 2005b; *Hill et al.*, 2015). As shown above and also below, the CP2k accretion parameterization is unique and appears superior to other parameterizations, but this parameterization is only used in a few microphysics schemes (e.g. WDM6 scheme in WRF, *Lim and Hong*, 2010).

Figure 9 compares the A_{c} calculated as a function of raindrop radius for all the accretion schemes under the conditions of $q_{\mathrm{c}} = 1$ g/kg, $R_{\mathrm{c}} = 10$ μm, $N_{\mathrm{r}} = 4000$ /m^3. It is obvious that the three schemes result in different relationships for the A_{c}. Considering the power-law form in the formula from the first method, i.e., the KK00 scheme in the control run and the Ko13 scheme, A_{c} is linearly related to raindrop radius in the logarithmic space. However, CP2k has an inflection point at 50 μm due to the piecewise function in Eq. 6. Under the condition of adequate cloud water, the accretion process in the KK00 or the Ko13 scheme only depends on the rain water mixing ratio. However, in CP2k, if the raindrop radius is less than 50 μm, the A_{c} is very small. As shown in Figure 9, the A_{c} in the KK00 or the Ko13 scheme is always larger than that in CP2k

when the raindrop radius is smaller than 2000 μm. The difference between CP2k and the other two schemes increases with decreasing raindrop radius; especially when the raindrop radius is smaller than 50 μm, with the maximum difference being more than two orders of magnitude. Therefore, the probability density distributions (PDFs) of raindrop radius are important for the difference between different accretion schemes.

Figure 10 shows the PDFs of raindrop radius used in the accretion process in the three schemes. All raindrops are smaller than 10^3 μm. The PDFs have peaks of ~30, ~30, and ~25 μm in the control run, Ko13, and CP2k, respectively, and the cumulative PDF shows that the raindrops with radius smaller than 50 μm have frequencies of 58.8%, 53.8%, and 46.0%, respectively. The drop size distributions from both aircraft observations and bin models also confirm that a large proportion of liquid droplets have radii larger than 25 μm but smaller than 50 μm (*Wood*, 2005a; *Morrison and Grabowski*, 2007). Such a large percentage of small raindrops makes the A_c and precipitation in CP2k quite different from that in other schemes (Figure 9). Furthermore, there is a positive feedback mechanism, since accretion increases q_r and A_c is positively correlated with q_r. The overestimation of the A_c in KK00 or Ko13 hence feeds back on itself. This is the reason why the precipitation and accretion rate differences between KK00 and CP2k are so large over the southeastern corner in domain 02 and during the second peak period in domain 03.

Previous studies have shown that to initiate liquid phase precipitation, the cloud effective radius needs to reach about 14 μm (*Rosenfeld et al.*, 2019). A closer look at

523 the cloud droplet sizes is hence informative to understand the differences in
524 precipitation behavior between CP2k and the other experiments. Figure 11 shows the
525 liquid-phase precipitation rate as a function of cloud droplet effective radius. The
526 liquid-phase precipitation rate is estimated as the product of total precipitation and the
527 ratio of liquid-phase process rates (autoconversion + accretion) and ice/mixed-phase
528 process rates (melting from snow + graupel). The liquid-phase precipitation rate
529 exceeds 2 mm/day when the cloud effective radius is 9 μm in the control run and Ko13.
530 In CP2k, it is not until the cloud effective radius reaches about 15 μm, that the
531 precipitation rate exceeds 2 mm/day. The contribution from autoconversion is close to
532 0 in the control run, which could be due to the consumption of cloud droplets by
533 accretion after droplets reach 9 μm. The value of 9 μm, is much smaller than 14 μm
534 needed to initiate liquid-phase precipitation, often suggested by observational studies
535 (*Rosenfeld et al.*, 2019). On the contrary, there is a significant increase in liquid-phase
536 precipitation rate from the autoconversion and accretion processes in CP2k at 15 μm.
537 Although A_{u} in CP2k is larger than that in other schemes, A_{c} ultimately determines
538 the liquid-phase precipitation rate, which has been discussed in many previous studies
539 (e.g., *Jiang et al.*, 2010; *Wood et al.*, 2009; *Michibata and Takemura*, 2015; *Gettelman*
540 *et al.*, 2015). The liquid-phase precipitation is suppressed by a weak A_{c}. Furthermore,
541 large A_{u} in CP2k can increase q_{r} but decrease q_{c}, which may enhance or suppress A_{c}
542 (*Posselt and Lohmann*, 2008). In other schemes, the accretion process is triggered to a
543 considerable amount with small liquid drops due to the overestimation of A_{c} when

544 confined to small drops. Therefore, the improvement in CP2k surface precipitation
545 compared to the control, appears to occur for the right reasons.
546
547 **4. Long-term analysis**
548 While the analysis of the single case study has allowed for an in-depth analysis, it
549 remains to be verified whether this case study is representative of the general behavior
550 of the model. As pointed out by *White et al.*, 2017), it is hard to be conclusive that one
551 scheme is better than others based on a few cases. Hence, one-month simulations are
552 performed from 0000 UTC 21 July to 0000 UTC 21 August 2014 with the same
553 domains in Figure 1, using the three accretion schemes (the control run, CP2k, and
554 Ko13). Only the results starting from 0000 UTC 22 July are analyzed. The horizontal
555 resolutions for domains 01, 02 and 03 are 30, 10 and 3.3 km, respectively; except for
556 the resolutions and simulation time, all other settings are the same as those in the two-
557 days simulations in Section 3.
558 Figure 12 shows the temporal evolution of the area-averaged daily precipitation
559 rate in domains 02 and 03 from the three accretion simulations and the observations.
560 Compared with the observed precipitation, the control run significantly overestimates
561 precipitation for most days, especially in domain 02. The average precipitation rate in
562 the observation, the control run, Ko13, and CP2k are, respectively, 1.56, 2.46, 2.49, and
563 2.17 mm/day over domain 02, and 4.54, 5.80, 5.87, and 5.17 mm/day over domain 03.
564 The results of Ko13 are very close to those in the control run, while CP2k significantly

565 reduces precipitation overprediction with *p*-values of student's t-test less than 0.01 for
566 both domain 02 and domain 03. Table 5 shows that CP2k has higher HSS scores than
567 the control run and Ko13 over both domains 02 and 03. Therefore, the effects of CP2k
568 on reducing precipitation overprediction are not limited to one specific case but appear
569 to be a plausible way to improve precipitation overprediction, at least of the Tibetan
570 Plateau.

571 The one-month simulations provide the opportunity to investigate the response of
572 the PDF of the surface precipitation to the changes of accretion schemes over the TP
573 region. The PDFs are based on the hourly precipitation rate from 0000 UTC 21 July to
574 0000 UTC 21 August 2014 with the three accretion schemes (the control run, CP2k,
575 and Ko13). As expected, Figure 13 shows that CP2k has more weak precipitation (<
576 ~0.2 mm/h) over both domains 02 and 03 than the control run and Ko13, corresponding
577 to the smaller total surface precipitation in CP2k. The results indicate that the PDF of
578 the surface precipitation is subject to the changes in the microphysical schemes over
579 the TP region. Furthermore, considering the significant climate effects of the TP region,
580 it is interesting to see whether microphysical schemes have significant effects on the
581 historical trend of precipitation intensity distribution with simulations over years in the
582 future research using the method in *Wang et al.* (2016).

583

584 **5. Sensitivity to horizontal resolution**

585 Different resolutions in the two simulations (case study from 22 to 23 July 2014

586 and long-term one-month simulation from 22 July to 21 August 2014) provide a good
587 opportunity to examine the effects of resolution on precipitation overprediction. The
588 area-averaged precipitation rate during the first two days (from 22 to 23 July) from the
589 one-month simulation is 0.36 mm/h in domain 03 with the resolution of 3.3 km (Figure
590 12b), which is larger than the 0.29 mm/h with the resolution of 1 km and the 0.24 mm/h
591 from the observations (Figure 6b). Similarly, the first two-days area-averaged
592 precipitation rate is 0.41 mm/h in domain 02 with the resolution of 10 km (Figure 12a),
593 larger than 0.32 mm/h with the resolution of 5 km and 0.21 mm/h from the observations
594 (Figure 6a). Furthermore, comparison with the precipitation in domains 02 and 03 also
595 provides some hints on the effects of resolutions. For the one case study, domain 02
596 with the resolution of 5 km (Figure 6a) overpredicts 51.5% of precipitation compared
597 with observations, and the number for domain 03 with the resolution of 1 km is only
598 20.8% (Figure 6b). For the one-month study, domains 02 and 03 overpredict
599 precipitation by 57.7% and 27.8%, respectively (Figure 12). These results confirm that
600 the model grid size plays an important role in the overprediction of precipitation over
601 the TP.

602 *Sato et al.* (2008) showed that a higher resolution simulation was more accurate in
603 reproducing the diurnal variation of precipitation, with precipitation rate more
604 consistent with observations. They claimed that higher resolution (< 7 km) may resolve
605 the convection initially occurred by the surface heating and consequently conduct a
606 proper simulation of the precipitation. *Xu et al.* (2012) found that the WRF simulations

607 at a resolution of 3 km could reproduce the timing of precipitation events but the
608 intensities were doubled. The first two-days comparison in our study shows that, when
609 the horizontal resolution increases from 3.3 km to 1 km, the simulation of precipitation
610 intensity can be effectively improved without affecting the trends of precipitation. This
611 indicates that 1 km or even higher resolution is needed to accurately simulate the
612 precipitation over the TP, possibly because such high resolutions can better resolve the
613 orography of this region.
614
615 **6. Summary and conclusions**
616 In this paper, a typical summer plateau precipitation event over the Tibetan Plateau
617 is simulated using the WRFv3.8.1 model with the Morrison double-moment scheme.
618 The control run reproduces the primary spatial distribution and temporal evolution of
619 precipitation rate. However, precipitation is significantly overestimated. To understand
620 the role of liquid-phase microphysical processes in the overprediction of precipitation,
621 sensitivity tests are conducted by introducing three parameterized liquid-phase
622 processes into the Morrison double-moment scheme, including three autoconversion
623 parameterizations (Be68, Bh94, and LD04), two accretion parameterizations (CP2k and
624 Ko13), and one entrainment-mixing parameterization (INHOMO).
625 The precipitation overprediction is significantly reduced with the accretion
626 scheme from *Cohard and Pinty* (2000). The Heidke skill scores with CP2k also show
627 better results compared to other cases. Furthermore, each simulation is further divided

into two parts: one with dominant ice/mixed-phase processes, the other with dominant liquid-phase processes. The simulations have the largest differences when the liquid-phase processes dominate, and the improvement in the CP2k experiment is more pronounced. When the ice/mixed-phase processes are important, all the simulations are equivalent, including CP2k. There are several reasons for this behavior. The accretion rate is smaller in the CP2k experiment than that in the control run, which suppresses precipitation due to liquid-phase processes. Due to weaker accretion, more cloud droplets remain suspended in the atmosphere and are available for riming onto snow and graupel. Precipitation due to melting from snow and graupel is then enhanced. The combination of the weaker accretion and stronger melting in CP2k offset each other. That is the reason why the precipitation does not change much in CP2k when ice/mixed-phase processes dominate. When the ice/mixed-phase processes are relatively weak, the precipitation from the enhanced riming and melting processes cannot compensate for the loss of precipitation due to the suppression of accretion. Therefore, the precipitation rate is smaller in CP2k than in the control run.

To understand the physical reasons for the improved performance of CP2k, the equations for parameterizing accretion rate in CP2k, KK00, and Ko13 are compared directly. The accretion rate in CP2k is always smaller than in the KK00 or the Ko13 scheme when the raindrop radius is smaller than 2000 μm. Furthermore, the difference increases with decreasing raindrop radius and can amount to more than two orders of magnitude when the raindrop radius is smaller than 50 μm. The PDFs of raindrop radii

649 have their peaks around 30 μm. Around 50% of raindrops have radius less than 50 μm.
650 This is the reason why CP2k suppresses accretion and liquid-phase precipitation
651 compared to the other two schemes. Further insight into the reasons for different
652 behavior in CP2k compared to the other schemes is provided through the relation of
653 cloud droplet size and liquid phase precipitation rates. It is often claimed that, to initiate
654 liquid-phase precipitation, the cloud effective radius needs to reach 14 μm. When the
655 cloud effective radius is 9 μm in the control run and Ko13, the liquid-phase precipitation
656 rate already exceeds 2 mm/day, however; in CP2k, on the other hand, liquid-phase
657 precipitation does not start until the effective radius reaches about 15 μm, which is more
658 consistent with observations.

659 The results in terms of precipitation sensitivity were confirmed in a long-term one-
660 month simulation as well. The time series of daily precipitation rate indicates that the
661 reduction in precipitation bias using CP2k is generally valid. CP2k also has the highest
662 HSS scores. Hence, it is assumed that the CP2k scheme generally produces more
663 accurate simulations of precipitation, at least over the Tibetan Plateau. More studies are
664 needed to understand whether these findings are applicable to regions beyond the
665 Tibetan Plateau as well. Theoretically, accretion is significantly affected by cloud
666 droplet and raindrop sizes, and these sizes are related to number concentrations and
667 liquid water mixing ratios of cloud droplets and raindrops. Therefore, it may be more
668 convincing to simultaneously consider number concentrations and liquid water mixing
669 ratios in the future development of the accretion parameterizations, similar to CP2k.

We also confirm that higher resolution simulations reduce precipitation overestimation compared to lower resolution simulations, as pointed out by previous studies (e.g., *Sato et al.*, 2008, *Xu et al.*, 2012). For the same simulation domains with different resolutions, the results in the high-resolution simulations are much closer to the observations.

It is noteworthy that small impacts of changing entrainment-mixing mechanisms and autoconversion schemes could be related to the cloud type in the Tibetan Plateau area. More studies are needed to further examine the impacts of these processes and accretion on cloud and precipitation under different conditions, with the ratio of accretion rate to autoconversion rate (*Wood*, 2005b; *Gettelman et al.*, 2013; *Lee and Baik*, 2017; *Michibata and Takemura*, 2015; *Seifert and Onishi*, 2016; *Jiang et al.*, 2010) and the entrainment-mixing parameterizations (*Lu et al.*, 2013). Furthermore, although our research shows the importance of the accretion process, it cannot be ignored that the ice-phase processes are also important in this region. Therefore, it is necessary to study the parameterizations of different ice-phase processes in the Tibetan Plateau area in the future.

Acknowledgements. The authors thank Prof. Amy Solomon for providing the microphysics scheme, Profs. Yinzhao Ma and Yang Hong for providing the precipitation data, and the data are available (https://data.mendeley.com/datasets/ynxtgtccj3/1. DOI: 10.17632/ynxtgtccj3.1). The

National Center for Environmental Prediction Final operational global analysis data were obtained online (https://rda.ucar.edu/datasets/ds083.2/index.html). Data from Clouds and the Earth's Radiant Energy System (CERES) project can be obtained online (https://ceres-tool.larc.nasa.gov/ord-tool/jsp/SYN1degEd41Selection.jsp). This research is supported by the National Key Research and Development Program of China (2018YFC1505702), the Second Tibetan Plateau Scientific Expedition and Research (STEP) program (2019QZKK0105), the Natural Science Foundation of Jiangsu Province (BK20160041), the National Natural Science Foundation of China (41822504, 91537108), the Qinglan Project (R2018Q05), and the Six Talent Peak Project in Jiangsu (2015-JY-011). Liu is supported by the U.S. Department of Energy Office of Science Biological and Environmental Research as part of the Atmospheric Systems Research (ASR) Program. Brookhaven National Laboratory is operated by Battelle for the U.S. Department of Energy under Contract DE-SC0012704.

Appendix A: Symbol List

N_c: number concentration of cloud droplets

q_c: mixing ratio of cloud droplet

N_r: number concentration of raindrops

q_r: mixing ratio of raindrops

N_i: number concentration of ice crystals

q_i: mixing ratio of ice crystals

712 N_s: number concentration of snow particles

713 q_s: mixing ratio of snow particles

714 N_g: number concentration of graupel particles

715 q_g: mixing ratio of graupel particles

716 A_u: conversion rate of accretion process

717 A_c: conversion rate of autoconversion process

718 ρ_a: air density

719 ε: dispersion

720 ρ_W: water density

721 λ: slope parameter

722 N_{c0}: number concentration of cloud water droplets before evaporation process

723 q_{c0}: mixing ratio of cloud water droplets before evaporation process

724 p_t: the threshold value of precipitation in the Heidke skill score

725 p_s: value of precipitation from simulations in the Heidke skill score

726 p_o: value of precipitation from observation in the Heidke skill score

727 τ: cloud optical depth

728 $\overline{r_e}$: averaged effective radius of cloud water droplets

729 LCWP: liquid cloud water path

730 EVAP-r: evaporation of raindrops

731 ACCR-r: accretion of cloud liquid water by rain

732 AUTO-r: autoconversion from cloud droplets to raindrops

MELT: melting from snow or graupel particles to raindrops

AUTO-s: autoconversion of cloud ice to snow

ACCR-s: accretion of cloud ice by snow

RIM-s: accretion of cloud droplets by snow particle

RIM-g: accretion of cloud droplets by graupel particle

Appendix B: Four Parameters in Equation (6)

In Equation (6), A_1, A_2, B_1, and B_2 are the functions related to two dispersion parameters of the gamma size distribution given by:

$$A_1 = \frac{\Gamma\left(\upsilon_c + 6/\alpha_c\right)}{\Gamma\left(\upsilon_c\right)} \tag{B1a}$$

$$B_1 = \frac{\Gamma\left(\upsilon_c + 3/\alpha_c\right)}{\Gamma\left(\upsilon_c\right)} \frac{\Gamma\left(\upsilon_r + 3/\alpha_r\right)}{\Gamma\left(\upsilon_r\right)} \tag{B1b}$$

$$A_2 = \frac{\Gamma\left(\upsilon_c + 9/\alpha_c\right)}{\Gamma\left(\upsilon_c\right)} \tag{B1c}$$

$$B_2 = \frac{\Gamma\left(\upsilon_c + 3/\alpha_c\right)}{\Gamma\left(\upsilon_c\right)} \frac{\Gamma\left(\upsilon_r + 6/\alpha_r\right)}{\Gamma\left(\upsilon_r\right)} \tag{B1d}$$

where υ and α are the two dispersion parameters in normalized form of cloud–raindrop size distributions $n(D) = N \frac{\alpha}{\Gamma(\upsilon)} \lambda^{\alpha\upsilon} D^{\alpha\upsilon-1} \exp[-(\lambda D)^{\alpha}]$; λ is the slope parameter; D and N represent diameter and total number concentration, respectively. Subscripts c and r in Eqs. (B1) represent cloud droplets and raindrops, respectively.

752 **Reference:**

753 Ashouri, H., K.-L. Hsu, S. Sorooshian, D. K. Braithwaite, K. R. Knapp, L. D. Cecil, B.
754 R. Nelson, and O. P. Prat (2015), PERSIANN-CDR: Daily precipitation climate
755 data record from multisatellite observations for hydrological and climate studies,
756 *Bulletin of the American Meteorological Society*, *96*(1), 69-83.
757 Barnston, A. G. (1992), Correspondence among the correlation, RMSE, and Heidke
758 forecast verification measures; refinement of the Heidke score, *Weather and*
759 *Forecasting*, *7*(4), 699-709.
760 Beheng, K. (1994), A parameterization of warm cloud microphysical conversion
761 processes, *Atmospheric Research*, *33*(1-4), 193-206.
762 Chen, B., Z. Hu, L. Liu, and G. Zhang (2017a), Raindrop Size Distribution
763 Measurements at 4,500 m on the Tibetan Plateau During TIPEX‐III, *Journal of*
764 *Geophysical Research: Atmospheres*, *122*(20), 11,092-011,106.
765 Chen, J., X. Wu, Y. Yin, Q. Huang, and H. Xiao (2017b), Characteristics of Cloud
766 Systems over the Tibetan Plateau and East China during Boreal Summer, *Journal*
767 *of Climate*, *30*(9), 3117-3137.
768 Chosson, F., J.-L. Brenguier, and L. Schüller (2007), Entrainment-mixing and radiative
769 transfer simulation in boundary layer clouds, *Journal of the atmospheric sciences*,
770 *64*(7), 2670-2682.
771 Cohard, J. M., and J. P. Pinty (2000), A comprehensive two‐moment warm
772 microphysical bulk scheme. I: Description and tests, *Quarterly Journal of the*

773 *Royal Meteorological Society*, *126*(566), 1815-1842.
774 Cooper, W. A., S. G. Lasher-Trapp, and A. M. Blyth (2013), The Influence of
775 Entrainment and Mixing on the Initial Formation of Rain in a Warm Cumulus
776 Cloud, *Journal of the Atmospheric Sciences*, *70*(6), 1727-1743, doi:10.1175/jas-d-
777 12-0128.1.
778 Ding, Y., Y. Zhang, Q. Ma, and G. Hu (2001), Analysis of the large-scale circulation
779 features and synoptic systems in East Asia during the intensive observation period
780 of GAME/HUBEX, *Journal of the Meteorological Society of Japan. Ser. II*,
781 *79*(1B), 277-300.
782 Fan, J., L. R. Leung, D. Rosenfeld, Q. Chen, Z. Li, J. Zhang, and H. Yan (2013),
783 Microphysical effects determine macrophysical response for aerosol impacts on
784 deep convective clouds, *Proc Natl Acad Sci U S A*, *110*(48), E4581-4590,
785 doi:10.1073/pnas.1316830110.
786 Fan, J., Y. Wang, D. Rosenfeld, and X. Liu (2016), Review of Aerosol–Cloud
787 Interactions: Mechanisms, Significance, and Challenges, *Journal of the*
788 *Atmospheric Sciences*, *73*(11), 4221-4252, doi:10.1175/jas-d-16-0037.1.
789 Flohn, H. (1957), Large-scale aspects of the “summer monsoon” in South and East Asia,
790 *Journal of the Meteorological Society of Japan. Ser. II*, *35*, 180-186.
791 Fu, Y., H. Li, and Y. Zi (2007), Case study of precipitation cloud structure viewed by
792 TRMM satellite in a valley of the Tibetan Plateau, *Plateau Meteorol*, *26*(1), 98-
793 106.

794 Fu, Y., G. Liu, G. Wu, R. Yu, Y. Xu, Y. Wang, R. Li, and Q. Liu (2006), Tower mast of
795 precipitation over the central Tibetan Plateau summer, *Geophysical Research*
796 *Letters*, *33*(5), doi:10.1029/2005gl024713.
797 Fujinami, H., and T. Yasunari (2001), The seasonal and intraseasonal variability of
798 diurnal cloud activity over the Tibetan Plateau, *Journal of the Meteorological*
799 *Society of Japan. Ser. II*, *79*(6), 1207-1227.
800 Gao, S., C. Lu, Y. Liu, F. Mei, J. Wang, L. Zhu, and S. Yan (2020), Contrasting Scale
801 Dependence of Entrainment‐Mixing Mechanisms in Stratocumulus Clouds,
802 *Geophysical Research Letters*, *47*(9), e2020GL086970.
803 Gao, W., L. Liu, J. Li, and C. Lu (2018), The Microphysical Properties of Convective
804 Precipitation Over the Tibetan Plateau by a Subkilometer Resolution Cloud‐
805 Resolving Simulation, *Journal of Geophysical Research: Atmospheres*, *123*(6),
806 3212-3227.
807 Gao, W., C. H. Sui, J. Fan, Z. Hu, and L. Zhong (2016), A study of cloud microphysics
808 and precipitation over the Tibetan Plateau by radar observations and cloud‐
809 resolving model simulations, *Journal of Geophysical Research: Atmospheres*,
810 *121*(22), 13,735-713,752.
811 Gerken, T., W. Babel, F. Sun, M. Herzog, Y. Ma, T. Foken, and H.-F. Graf (2013),
812 Uncertainty in atmospheric profiles and its impact on modeled convection
813 development at Nam Co Lake, Tibetan Plateau, *Journal of Geophysical Research:*
814 *Atmospheres*, *118*(22), 12,317-312,331, doi:10.1002/2013jd020647.

Gettelman, A., H. Morrison, S. Santos, P. Bogenschutz, and P. M. Caldwell (2015), Advanced Two-Moment Bulk Microphysics for Global Models. Part II: Global Model Solutions and Aerosol–Cloud Interactions, *Journal of Climate*, *28*(3), 1288-1307, doi:10.1175/jcli-d-14-00103.1.

Gettelman, A., H. Morrison, C. R. Terai, and R. Wood (2013), Microphysical process rates and global aerosol–cloud interactions, *Atmospheric Chemistry and Physics*, *13*(19), 9855-9867, doi:10.5194/acp-13-9855-2013.

Grabowski, W. W. (2006), Indirect impact of atmospheric aerosols in idealized simulations of convective–radiative quasi equilibrium, *Journal of climate*, *19*(18), 4664-4682.

Grabowski, W. W., and H. Morrison (2011), Indirect Impact of Atmospheric Aerosols in Idealized Simulations of Convective–Radiative Quasi Equilibrium. Part II: Double-Moment Microphysics, *Journal of Climate*, *24*(7), 1897-1912, doi:10.1175/2010jcli3647.1.

Hahn, D. G., and S. Manabe (1975), The role of mountains in the south Asian monsoon circulation, *Journal of the Atmospheric Sciences*, *32*(8), 1515-1541.

Hill, A. A., G. Feingold, and H. Jiang (2009), The Influence of Entrainment and Mixing Assumption on Aerosol–Cloud Interactions in Marine Stratocumulus, *Journal of the Atmospheric Sciences*, *66*(5), 1450-1464, doi:10.1175/2008jas2909.1.

Hill, A. A., B. J. Shipway, and I. A. Boutle (2015), How sensitive are aerosol-precipitation interactions to the warm rain representation?, *Journal of Advances in*

836 *Modeling Earth Systems*, *7*(3), 987-1004, doi:10.1002/2014ms000422.
837 Hoffmann, F., and G. Feingold (2019), Entrainment and Mixing in Stratocumulus:
838 Effects of a New Explicit Subgrid-Scale Scheme for Large-Eddy Simulations with
839 Particle-Based Microphysics, *Journal of the Atmospheric Sciences*, *76*(7), 1955-
840 1973, doi:10.1175/jas-d-18-0318.1.
841 Hsu, H. H., and X. Liu (2003), Relationship between the Tibetan Plateau heating and
842 East Asian summer monsoon rainfall, *Geophysical Research Letters*, *30*(20).
843 Huffman, G. J., D. T. Bolvin, E. J. Nelkin, D. B. Wolff, R. F. Adler, G. Gu, Y. Hong, K.
844 P. Bowman, and E. F. Stocker (2007), The TRMM multisatellite precipitation
845 analysis (TMPA): Quasi-global, multiyear, combined-sensor precipitation
846 estimates at fine scales, *Journal of hydrometeorology*, *8*(1), 38-55.
847 Jiang, H., G. Feingold, and A. Sorooshian (2010), Effect of aerosol on the susceptibility
848 and efficiency of precipitation in warm trade cumulus clouds, *Journal of the*
849 *atmospheric sciences*, *67*(11), 3525-3540.
850 Jiang, J. H., B. Wang, K. Goya, K. Hocke, S. D. Eckermann, J. Ma, D. L. Wu, and W.
851 G. Read (2004), Geographical distribution and interseasonal variability of tropical
852 deep convection: UARS MLS observations and analyses, *Journal of Geophysical*
853 *Research: Atmospheres*, *109*(D3), n/a-n/a, doi:10.1029/2003jd003756.
854 Jing, X., and K. Suzuki (2018), The Impact of Process‐Based Warm Rain Constraints
855 on the Aerosol Indirect Effect, *Geophysical Research Letters*, *45*(19), 10,729-
856 710,737.

857 Jing, X., K. Suzuki, and T. Michibata (2019), The key role of warm rain
858 parameterization in determining the aerosol indirect effect in a global climate
859 model, *Journal of Climate*, *32*(14), 4409-4430.
860 Joyce, R. J., J. E. Janowiak, P. A. Arkin, and P. Xie (2004), CMORPH: A method that
861 produces global precipitation estimates from passive microwave and infrared data
862 at high spatial and temporal resolution, *Journal of hydrometeorology*, *5*(3), 487-
863 503.
864 Khairoutdinov, M., and Y. Kogan (2000), A new cloud physics parameterization in a
865 large-eddy simulation model of marine stratocumulus, *Monthly weather review*,
866 *128*(1), 229-243.
867 Kogan, Y. (2013), A cumulus cloud microphysics parameterization for cloud-resolving
868 models, *Journal of the Atmospheric Sciences*, *70*(5), 1423-1436.
869 Kollias, P., and B. Albrecht (2000), The Turbulence Structure in a Continental
870 Stratocumulus Cloud from Millimeter-Wavelength Radar Observations, *Journal*
871 *of the Atmospheric Sciences*, *57*(15), 2417-2434, doi:10.1175/1520-
872 0469(2000)057<2417:ttsiac>2.0.co;2.
873 Kurosaki, Y., and F. Kimura (2002), Relationship between topography and daytime
874 cloud activity around Tibetan Plateau, *Journal of the Meteorological Society of*
875 *Japan. Ser. II*, *80*(6), 1339-1355.
876 Lasher-Trapp, S. G., W. A. Cooper, and A. M. Blyth (2005), Broadening of droplet size
877 distributions from entrainment and mixing in a cumulus cloud, *Quarterly Journal*

878 *of the Royal Meteorological Society*, *131*(605), 195-220, doi:10.1256/qj.03.199.
879 Lee, H., and J.-J. Baik (2017), A Physically Based Autoconversion Parameterization,
880 *Journal of the Atmospheric Sciences*, *74*(5), 1599-1616, doi:10.1175/jas-d-16-
881 0207.1.
882 Li, G., Y. Wang, and R. Zhang (2008a), Implementation of a two-moment bulk
883 microphysics scheme to the WRF model to investigate aerosol-cloud interaction,
884 *Journal of Geophysical Research-Atmospheres*, *113*(D15),
885 doi:10.1029/2007jd009361.
886 Li, J., J. Chen, C. Lu, and X. Wu (2020), Impacts of TIPEX‐III Rawinsondes on the
887 Dynamics and Thermodynamics over the Eastern Tibetan Plateau in the Boreal
888 Summer, *Journal of Geophysical Research: Atmospheres*, e2020JD032635.
889 Li, J., L.-g. You, Z.-j. Hu, D.-b. Tu, and L.-g. Li (2006), Analysis on raindrop-size
890 distribution characteristics of Maqu region in upper reach of Yellow River, *Plateau*
891 *Meteorology*, *25*(5), 942-949.
892 Li, R., Q. Min, X. Wu, and Y. Fu (2013), Retrieving latent heating vertical structure
893 from cloud and precipitation profiles-Part II: Deep convective and stratiform rain
894 processes, *Journal Of Quantitative Spectroscopy & Radiative Transfer*, *122*, 47-
895 63, doi:10.1016/j.jqsrt.2012.11.029.
896 Li, Y., Y. Wang, Y. Song, L. Hu, S. Gao, and F. Rong (2008b), Characteristics of
897 Summer Convective Systems Initiated over the Tibetan Plateau. Part I: Origin,
898 Track, Development, and Precipitation, *Journal of Applied Meteorology and*

899 *Climatology*, *47*(10), 2679-2695, doi:10.1175/2008jamc1695.1.
900 Li, Y., and M. Zhang (2016), Cumulus over the Tibetan Plateau in the Summer Based
901 on CloudSat-CALIPSO Data, *Journal Of Climate*, *29*(3), 1219-1230,
902 doi:10.1175/jcli-d-15-0492.1.
903 Li, Y., and M. Zhang (2017), The Role of Shallow Convection over the Tibetan Plateau,
904 *Journal of Climate*, *30*(15), 5791-5803, doi:10.1175/jcli-d-16-0599.1.
905 Lim, K.-S. S., and S.-Y. Hong (2010), Development of an Effective Double-Moment
906 Cloud Microphysics Scheme with Prognostic Cloud Condensation Nuclei (CCN)
907 for Weather and Climate Models, *Monthly Weather Review*, *138*(5), 1587-1612,
908 doi:10.1175/2009mwr2968.1.
909 Liu, X., et al. (2011), Testing cloud microphysics parameterizations in NCAR CAM5
910 with ISDAC and M-PACE observations, *Journal of Geophysical Research*, *116*,
911 doi:10.1029/2011jd015889.
912 Liu, Y. (2005), Size truncation effect, threshold behavior, and a new type of
913 autoconversion parameterization, *Geophysical Research Letters*, *32*(11),
914 doi:10.1029/2005gl022636.
915 Liu, Y., and P. H. Daum (2004), Parameterization of the autoconversion process. Part I:
916 Analytical formulation of the Kessler-type parameterizations, *Journal of the*
917 *atmospheric sciences*, *61*(13), 1539-1548.
918 Lu, C., Y. Liu, S. Niu, S. Krueger, and T. Wagner (2013), Exploring parameterization
919 for turbulent entrainment-mixing processes in clouds, *Journal of Geophysical*

920 *Research: Atmospheres*, *118*(1), 185-194, doi:10.1029/2012jd018464.
921 Luo, H., and M. Yanai (1983), The large-scale circulation and heat sources over the
922 Tibetan Plateau and surrounding areas during the early summer of 1979. Part I:
923 Precipitation and kinematic analyses, *Monthly Weather Review*, *111*(5), 922-944.
924 Luo, H., and M. Yanai (1984), The large-scale circulation and heat sources over the
925 Tibetan Plateau and surrounding areas during the early summer of 1979. Part II:
926 Heat and moisture budgets, *Monthly Weather Review*, *112*(5), 966-989.
927 Ma, Y., Y. Hong, Y. Chen, Y. Yang, G. Tang, Y. Yao, D. Long, C. Li, Z. Han, and R. Liu
928 (2018), Performance of Optimally Merged Multisatellite Precipitation Products
929 Using the Dynamic Bayesian Model Averaging Scheme Over the Tibetan Plateau,
930 *Journal of Geophysical Research: Atmospheres*, *123*(2), 814-834,
931 doi:10.1002/2017jd026648.
932 Maussion, F., D. Scherer, R. Finkelnburg, J. Richters, W. Yang, and T. Yao (2011), WRF
933 simulation of a precipitation event over the Tibetan Plateau, China – an assessment
934 using remote sensing and ground observations, *Hydrology and Earth System*
935 *Sciences*, *15*(6), 1795-1817, doi:10.5194/hess-15-1795-2011.
936 Michibata, T., and T. Takemura (2015), Evaluation of autoconversion schemes in a
937 single model framework with satellite observations, *Journal of Geophysical*
938 *Research: Atmospheres*, *120*(18), 9570-9590.
939 Molnar, P., W. R. Boos, and D. S. Battisti (2010), Orographic controls on climate and
940 paleoclimate of Asia: thermal and mechanical roles for the Tibetan Plateau, *Annual*

941 *Review of Earth and Planetary Sciences*, *38*, 77-102.
942 Morrison, H., J. A. Curry, and V. I. Khvorostyanov (2005), A new double-moment
943 microphysics parameterization for application in cloud and climate models. Part I:
944 Description, *J. Atmos. Sci.*, *62*(6), 1665-1677, doi:10.1175/JAS3446.1.
945 Morrison, H., and W. W. Grabowski (2007), Comparison of Bulk and Bin Warm-Rain
946 Microphysics Models Using a Kinematic Framework, *Journal of the Atmospheric*
947 *Sciences*, *64*(8), 2839-2861, doi:10.1175/jas3980.
948 Morrison, H., and W. W. Grabowski (2008), Modeling Supersaturation and Subgrid-
949 Scale Mixing with Two-Moment Bulk Warm Microphysics, *Journal of the*
950 *Atmospheric Sciences*, *65*(3), 792-812, doi:10.1175/2007jas2374.1.
951 Morrison, H., J. A. Milbrandt, G. H. Bryan, K. Ikeda, S. A. Tessendorf, and G.
952 Thompson (2015), Parameterization of Cloud Microphysics Based on the
953 Prediction of Bulk Ice Particle Properties. Part II: Case Study Comparisons with
954 Observations and Other Schemes, *Journal of the Atmospheric Sciences*, *72*(1),
955 312-339, doi:10.1175/jas-d-14-0066.1.
956 Nitta, T. (1983), Observational study of heat sources over the eastern Tibetan Plateau
957 during the summer monsoon, *Journal of the Meteorological Society of Japan. Ser.*
958 *II*, *61*(4), 590-605.
959 Porcù, F., L. P. D'Adderio, F. Prodi, and C. Caracciolo (2014), Rain drop size
960 distribution over the Tibetan Plateau, *Atmospheric research*, *150*, 21-30.
961 Posselt, R., and U. Lohmann (2008), Introduction of prognostic rain in ECHAM5:

962 design and single column model simulations, *Atmospheric Chemistry and Physics*,
963 *8*(11), 2949-2963.
964 Qie, X., X. Kong, G. Zhang, T. Zhang, T. Yuan, Y. Zhou, Y. Zhang, H. Wang, and A.
965 Sun (2005), The possible charge structure of thunderstorm and lightning
966 discharges in northeastern verge of Qinghai–Tibetan Plateau, *Atmospheric*
967 *Research*, *76*(1-4), 231-246.
968 Qie, X., X. Wu, T. Yuan, J. Bian, and D. Lu (2014), Comprehensive pattern of deep
969 convective systems over the Tibetan Plateau–South Asian monsoon region based
970 on TRMM data, *Journal of climate*, *27*(17), 6612-6626.
971 Rosenfeld, D., Y. Zhu, M. Wang, Y. Zheng, T. Goren, and S. Yu (2019), Aerosol-driven
972 droplet concentrations dominate coverage and water of oceanic low-level clouds,
973 *Science*, *363*(6427), eaav0566.
974 Sato, T., T. Yoshikane, M. Satoh, H. MIURA, and H. Fujinami (2008), Resolution
975 dependency of the diurnal cycle of convective clouds over the Tibetan Plateau in
976 a mesoscale model, *Journal of the Meteorological Society of Japan. Ser. II*, *86*, 17-
977 31.
978 Seifert, A., and R. Onishi (2016), Turbulence effects on warm-rain formation in
979 precipitating
980 shallow convection revisited, *Atmospheric Chemistry and Physics*, *16*(18), 12127-
981 12141, doi:10.5194/acp-16-12127-2016.
982 Shen, R., E. R. Reiter, and J. F. Bresch (1986), Some aspects of the effects of sensible

983 heating on the development of summer weather systems over the Tibetan Plateau,
984 *Journal of the atmospheric sciences*, *43*(20), 2241-2260.
985 Slawinska, J., W. W. Grabowski, H. Pawlowska, and H. Morrison (2012), Droplet
986 Activation and Mixing in Large-Eddy Simulation of a Shallow Cumulus Field,
987 *Journal of the Atmospheric Sciences*, *69*(2), 444-462, doi:10.1175/jas-d-11-054.1.
988 Slawinska, J., W. W. Grabowski, H. Pawlowska, and A. A. Wyszogrodzki (2008),
989 Optical Properties of Shallow Convective Clouds Diagnosed from a Bulk-
990 Microphysics Large-Eddy Simulation, *Journal of Climate*, *21*(7), 1639-1647,
991 doi:10.1175/2007jcli1820.1.
992 Tang, J., X. Guo, and Y. Chang (2019), A numerical investigation on microphysical
993 properties of clouds and precipitation over the Tibetan Plateau in summer 2014,
994 *Journal of Meteorological Research*, *33*(3), 463-477.
995 Ueda, H., H. Kamahori, and N. Yamazaki (2003), Seasonal contrasting features of heat
996 and moisture budgets between the eastern and western Tibetan Plateau during the
997 GAME IOP, *Journal of climate*, *16*(14), 2309-2324.
998 Ueda, H., and T. Yasunari (1998), Role of warming over the Tibetan Plateau in early
999 onset of the summer monsoon over the Bay of Bengal and the South China Sea,
1000 *Journal of the Meteorological Society of Japan. Ser. II*, *76*(1), 1-12.
1001 Wang, B., Q. Bao, B. Hoskins, G. Wu, and Y. Liu (2008), Tibetan Plateau warming and
1002 precipitation changes in East Asia, *Geophysical Research Letters*, *35*(14).
1003 Wang, M., et al. (2012), Constraining cloud lifetime effects of aerosols using A-Train

satellite observations, *Geophysical Research Letters*, *39*(15), doi:10.1029/2012gl052204.

Wang, W., Y.-H. Kuo, and T. T. Warner (1993), A diabatically driven mesoscale vortex in the lee of the Tibetan Plateau, *Monthly weather review*, *121*(9), 2542-2561.

Wang, Y., J. Fan, R. Zhang, L. R. Leung, and C. Franklin (2013), Improving bulk microphysics parameterizations in simulations of aerosol effects, *Journal of Geophysical Research: Atmospheres*, *118*(11), 5361-5379, doi:10.1002/jgrd.50432.

Wang, Y., P. Ma, J. H. Jiang, H. Su, and P. J. Rasch (2016), Toward reconciling the influence of atmospheric aerosols and greenhouse gases on light precipitation changes in Eastern China, *Journal of Geophysical Research*, *121*(10), 5878-5887.

Wang, Y., S. Niu, C. Lu, Y. Liu, J. Chen, and W. Yang (2019a), An Observational Study on Cloud Spectral Width in North China, *Atmosphere*, *10*(3), 109, doi:10.3390/atmos10030109.

Wang, Y., S. Niu, J. Lv, C. Lu, X. Xu, Y. Wang, J. Ding, H. Zhang, T. Wang, and B. Kang (2019b), A New Method for Distinguishing Unactivated Particles in Cloud Condensation Nuclei Measurements: Implications for Aerosol Indirect Effect Evaluation, *Geophysical Research Letters*, doi:10.1029/2019gl085379.

White, B., E. Gryspeerdt, P. Stier, H. Morrison, G. Thompson, and Z. Kipling (2017), Uncertainty from the choice of microphysics scheme in convection-permitting models significantly exceeds aerosol effects, *Atmospheric Chemistry and Physics*,

17(19), 12145-12175, doi:10.5194/acp-17-12145-2017.

Wood, R. (2005a), Drizzle in stratiform boundary layer clouds. Part I: Vertical and horizontal structure, *Journal of the Atmospheric Sciences*, *62*(9), 3011-3033.

Wood, R. (2005b), Drizzle in stratiform boundary layer clouds. Part II: Microphysical aspects, *Journal of the atmospheric sciences*, *62*(9), 3034-3050.

Wood, R., T. L. Kubar, and D. L. Hartmann (2009), Understanding the Importance of Microphysics and Macrophysics for Warm Rain in Marine Low Clouds. Part II: Heuristic Models of Rain Formation, *Journal of the Atmospheric Sciences*, *66*(10), 2973-2990, doi:10.1175/2009jas3072.1.

Wu, G. X., and S. J. Chen (1985), The effect of mechanical forcing on the formation of a mesoscale vortex, *Quarterly Journal of the Royal Meteorological Society*, *111*(470), 1049-1070.

Wu, Y., and L. Liu (2017), Statistical characteristics of raindrop size distribution in the Tibetan Plateau and southern China, *Advances in Atmospheric Sciences*, *34*(6), 727-736.

Xie, X., and X. Liu (2011), Effects of spectral dispersion on clouds and precipitation in mesoscale convective systems, *Journal of Geophysical Research: Atmospheres*, *116*(D6).

Xie, X., X. Liu, Y. Peng, Y. Wang, Z. Yue, and X. Li (2013), Numerical simulation of clouds and precipitation depending on different relationships between aerosol and cloud droplet spectral dispersion, *Tellus Series B-Chemical and Physical*

1046 *Meteorology*, *65*, doi:10.3402/tellusb.v65i0.19054.
1047 Xu, J., B. Zhang, M. Wang, and H. Wang (2012), Diurnal variation of summer
1048 precipitation over the Tibetan Plateau: a cloud-resolving simulation, paper
1049 presented at Annales Geophysicae, Copernicus GmbH.
1050 Yanai, M., and C. Li (1994), Mechanism of heating and the boundary layer over the
1051 Tibetan Plateau, *Monthly Weather Review*, *122*(2), 305-323.
1052 Yanai, M., C. Li, and Z. Song (1992), Seasonal heating of the Tibetan Plateau and its
1053 effects on the evolution of the Asian summer monsoon, *Journal of the*
1054 *Meteorological Society of Japan. Ser. II*, *70*(1B), 319-351.
1055 Yang, K., H. Wu, J. Qin, C. Lin, W. Tang, and Y. Chen (2014), Recent climate changes
1056 over the Tibetan Plateau and their impacts on energy and water cycle: A review,
1057 *Global and Planetary Change*, *112*, 79-91.
1058 Ye, D. (1981), Some characteristics of the summer circulation over the Qinghai-Xizang
1059 (Tibet) Plateau and its neighborhood, *Bulletin of the American Meteorological*
1060 *Society*, *62*(1), 14-19.
1061 Yeh, T. C. (1950), The circulation of the high troposphere over China in the winter of
1062 1945–46, *Tellus*, *2*(3), 173-183.
1063 Yin, Z.-Y., X. Zhang, X. Liu, M. Colella, and X. Chen (2008), An assessment of the
1064 biases of satellite rainfall estimates over the Tibetan Plateau and correction
1065 methods based on topographic analysis, *Journal of Hydrometeorology*, *9*(3), 301-
1066 326.

1067 Zhao, C., L. Liu, Q. Wang, Y. Qiu, Y. Wang, and X. Wu (2017), MMCR-based
1068 characteristic properties of non-precipitating cloud liquid droplets at Naqu site
1069 over Tibetan Plateau in July 2014, *Atmospheric Research*, *190*, 68-76,
1070 doi:10.1016/j.atmosres.2017.02.002.
1071 Zhao, C., X. Tie, G. Brasseur, K. J. Noone, T. Nakajima, Q. Zhang, R. Zhang, M. Huang,
1072 Y. Duan, and G. Li (2006), Aircraft measurements of cloud droplet spectral
1073 dispersion and implications for indirect aerosol radiative forcing, *Geophysical*
1074 *research letters*, *33*(16).
1075
1076 **Caption List:**
1077 **Table 1.** Summary of case names and corresponding formulations for the seven
1078 experiments. The meaning of each symbol and references for each case can be found in
1079 the text.
1080 **Table 2.** Contingency table used to calculate the Heidke skill score (HSS). The elements
1081 *a-d* represent the numbers of "hits", "false alarms", "misses" and "correct negatives",
1082 respectively. p_t is the threshold value of precipitation in observation and simulations, p_s
1083 is the value from simulations and p_o is the value from observations.
1084 **Table 3.** The values of four elements *a-d* and Heidke skill score (HSS) for all
1085 simulations over domain 02 and domain 03 (d02/d03) of the control run, Be68, Bh94,
1086 LD04 (different autoconversion schemes), CP2k, Ko13 (different accretion schemes)
1087 and INHOMO run (different mixing mechanism).

1088 **Table 4.** The area-averaged liquid cloud water path LCWP (g/m^2), mean effective
1089 radius $\overline{r_e}$ (μm) and number concentration N_c ($/cm^3$) of cloud droplets over domains 02
1090 and 03 (d02/d03) of the control run, Be68, Bh94, LD04 (different autoconversion
1091 schemes), CP2k, Ko13 (different accretion schemes) and INHOMO run (different
1092 mixing mechanism). The observation results from Clouds and the Earth's Radiant
1093 Energy System (CERES) are also shown.

1094 **Table 5.** The values of four elements *a-d* and Heidke skill score (HSS) for three one-
1095 month simulations over domain 02 and domain 03 of the control run and CP2k, Ko13
1096 (different accretion schemes).

1097

1098 **Figure 1.** Geographic locations of the three domains used in the numerical simulation.
1099 The color bar represents the height (m) above the sea level.

1100 **Figure 2.** Spatial distributions of 48 h accumulated precipitation (mm) during 0000
1101 UTC 22 July to 0000 UTC 24 July 2014 from the observations and the control run over
1102 domain 02 (a, b) and domain 03 (c, d).

1103 **Figure 3.** Time series of area-averaged hourly precipitation rate (mm/h) during 0000
1104 UTC 22 July to 0000 UTC 24 July 2014 over (a) domain 02 and (b) domain 03 from
1105 the observations and the control run.

1106 **Figure 4.** Mean vertical profiles of mixing ratios (g/kg) of cloud droplets (q_c),
1107 raindrops(q_r), ice particles(q_i), snow particles (q_s), graupel particles(q_g) and their
1108 primary microphysical processes in the control run (a, b) averaged from 48 h over

domain 02 except southeastern corner, (c, d)averaged from 48 h at southeastern corner over domain 02, averaged during two precipitation peaks (e, f) 0700-1200 UTC 22 July 2014 and (g, h) 0700-1200 UTC 23 July 2014 over domain 03. The purple dot-dash lines denote the mean height of 0 ℃ isotherm.

Figure 5. Spatial distributions of 48 h accumulated precipitation (mm) during 0000 UTC 22 July to 0000 UTC 24 July 2014 from observations and all sensitivity simulations over (a-f) domain 02 and domain 03.

Figure 6. Time series of area-averaged hourly precipitation rate (mm/h) during 0000 UTC 22 July to 0000 UTC 24 July 2014 over (a) domain 02 and (b) domain 03 from the observations and all simulations.

Figure 7. The time series of area-averaged autoconversion rate, accretion rate, and the ratio of accretion rate to autoconversion rate (A_c/A_u) over (a, c, e) domain 02 and (b, d, f) domain 03 for all simulations, respectively.

Figure 8. Differences of mean vertical profiles of the dominated microphysical processes conversion rates between CP2k and the control run (CP2k-Control) from (a) domain 02 except southeastern corner, (b) the southeastern corner of domain 02, and during the two precipitation peak periods (c) 0700-1200 UTC 22 July and (d) 0700-1200 UTC 23 July over domain 03. The purple dot-dash lines denote the mean height of 0 ℃ isotherm.

Figure 9. The accretion rate as a function of raindrop radius with fixed cloud mixing ratio q_c = 1 g/kg, the radius of cloud droplet R_c = 10 μm, number concentration of raindrops N_r = 4000 /m^3 for the three accretion schemes.

Figure 10. Probability distribution function (PDF) and cumulative PDF of raindrop radius involved in the accretion process for (a) the control run, (b) CP2k, and (c) Ko13. The purple line denotes the radius of raindrop equal to 50 μm.

Figure 11. Dependence of warm rain intensity on cloud effective radius from the control run and CP2k during 0000 UTC 22 July to 0000 UTC 24 July 2014 over domain 03.

Figure 12. Time series of area-averaged daily precipitation rate (mm/day) from 0000 UTC 22 July to 0000 UTC 20 August 2014 over (a) domain 02 and (b) domain 03 in the observations and three accretion cases (the control run, CP2k and Ko13).

Figure 13. Probability distribution function (PDF) of precipitation rate (mm/h) from 0000 UTC 21 July to 0000 UTC 21 August 2014 over (a) domain 02 and (b) domain 03 in the three accretion cases (the control run, CP2k and Ko13).

1145 Table 1. Summary of case names and corresponding formulations for the seven
1146 experiments. The meaning of each symbol and references for each case can be found in
1147 the text.
1148

Liquid-phase process	Case name	Formulations
-	Control run	$A_u = 1350 \times q_c^{2.47}(N_c \times 10^{-6^{-1.79}}\rho_a^{-1.47}$ $A_c = 67 \times (q_c q_r)^{1.15}\rho_a^{-2.3}$
Autoconversion	Be68	$A_u = \frac{3.5 \times 10^{-2} q_c^2}{0.12 + 1.0 \times 10^{-12}\frac{N_c}{q_c}}$
	Bh94	$A_u = 6.0 \times 10^{28} n^{-1.7}(q_c \times 10^{-3})^{4.7}(N_c \times 10^{-6})^{-3.3}$
	LD04	$A_u = 1.1 \times 10^{13}\left[\frac{(1+3\varepsilon^2)(1+4\varepsilon^2)(1+5\varepsilon^2)}{(1+\varepsilon^2)(1+2\varepsilon^2)}\frac{q_c^3}{N_c}\right]$ $\times \frac{1}{2}(x_c^2 + 2x_c + 2)(1+x_c)e^{-2x_c}$
Accretion	Ko13	$A_c = 8.53 \times q_c^{1.05} {q_r}^{0.98}\rho_a^{-2.03}$
	CP2k	$A_c = \frac{\pi}{6}\rho_W \rho_a K_1 \frac{N_c N_r}{\lambda_c^3}\left(\frac{A1}{\lambda_c^3} + \frac{B1}{\lambda_r^3}\right)$, $if\ R_r \geq 50\mu m$, and $A_c = \frac{\pi}{6}\rho_W \rho_a K_2 \frac{N_c N_r}{\lambda_c^3}\left(\frac{A2}{\lambda_c^6} + \frac{B2}{\lambda_r^6}\right)$, $if\ R_r < 50\mu m$.
Entrainment-mixing	INHOMO	$N_c = N_{c0}\left(\frac{q_c}{q_{c0}}\right)^{\alpha}$, $\alpha = 1$.

1149
1150

Table 2. Contingency table used to calculate the Heidke skill score (HSS). The elements *a*-*d* represent the numbers of "hits", "false alarms", "misses" and "correct negatives", respectively. p_t is the threshold value of precipitation in observation and simulations, p_s is the value from simulations and p_o is the value from observations.

	Observation $p_o > p_t$	Observation $p_o \leq p_t$
Simulation $p_s > p_t$	*a*	*b*
Simulation $p_s \leq p_t$	*c*	*d*

Table 3. The values of four elements *a*-*d* and Heidke skill score (HSS) for all simulations over domain 02 and domain 03 (d02/d03) of the control run, Be68, Bh94, LD04 (different autoconversion schemes), CP2k, Ko13 (different accretion schemes) and INHOMO run (different mixing mechanism).

	a	*b*	*c*	*d*	HSS
Control	2636/304	1224/148	773/76	2231/48	0.419/0.049
Autoconversion					
Be68	2645/309	1261/142	764/71	2194/54	0.411/0.097
Bh94	2533/306	1148/138	876/74	2307/58	0.411/0.110
LD04	2628/313	1264/154	781/67	2191/42	0.405/0.043
Accretion					
CP2k	2583/304	1063/129	632/76	2586/67	0.508/0.152
K013	2620/303	1223/146	770/77	2251/50	0.420/0.057
Mixing mechanism					
INHOMO	2656/308	1124/141	753/72	2214/55	0.420/0.100

Table 4. The area-averaged liquid cloud water path LCWP (g/m^2), mean effective radius $\overline{r_e}$ (μm) and number concentration N_c ($/cm^3$) of cloud droplets over domains 02 and 03 (d02/d03) of the control run, Be68, Bh94, LD04 (different autoconversion schemes), CP2k, Ko13 (different accretion schemes) and INHOMO run (different mixing mechanism). The observation results from Clouds and the Earth's Radiant Energy System (CERES) are also shown.

	LCWP(g/m^2)	$\overline{r_e}$ (μm)	N_c($/cm^3$)
Control	73.5/66.8	6.97/6.77	71.5/91.2
Autoconversion			
Be68	63.4/59.4	6.84/6.74	71.3/91.6
Bh94	81.3/76.1	7.13/7.01	72.3/91.9
LD04	63.8/60.9	6.85/6.69	71.6/91.3
Accretion			
CP2k	121.0/97.0	7.52/7.15	72.4/90.1
Ko13	74.4/64.4	6.92/6.72	71.5/91.0
Mixing mechanism			
INHOMO	72.9/66.7	7.03/6.87	68.9/86.3
Observation			
CERES	100.4/91.2	9.13/8.75	-

1172 Table 5. The values of four elements *a-d* and Heidke skill score (HSS) for three one-
1173 month simulations over domain 02 and domain 03 of the control run and CP2k, Ko13
1174 (different accretion schemes).

	a	*b*	*c*	*d*	HSS
domain 02					
Control	3780	5052	1924	24584	0.403
CP2k	3749	4369	1955	25267	0.435
Ko13	3764	4825	1940	24811	0.413
domain 03					
Control	1188	2856	93	2538	0.220
CP2k	1163	2355	118	3084	0.262
Ko13	1181	2908	100	2531	0.211

1175
1176

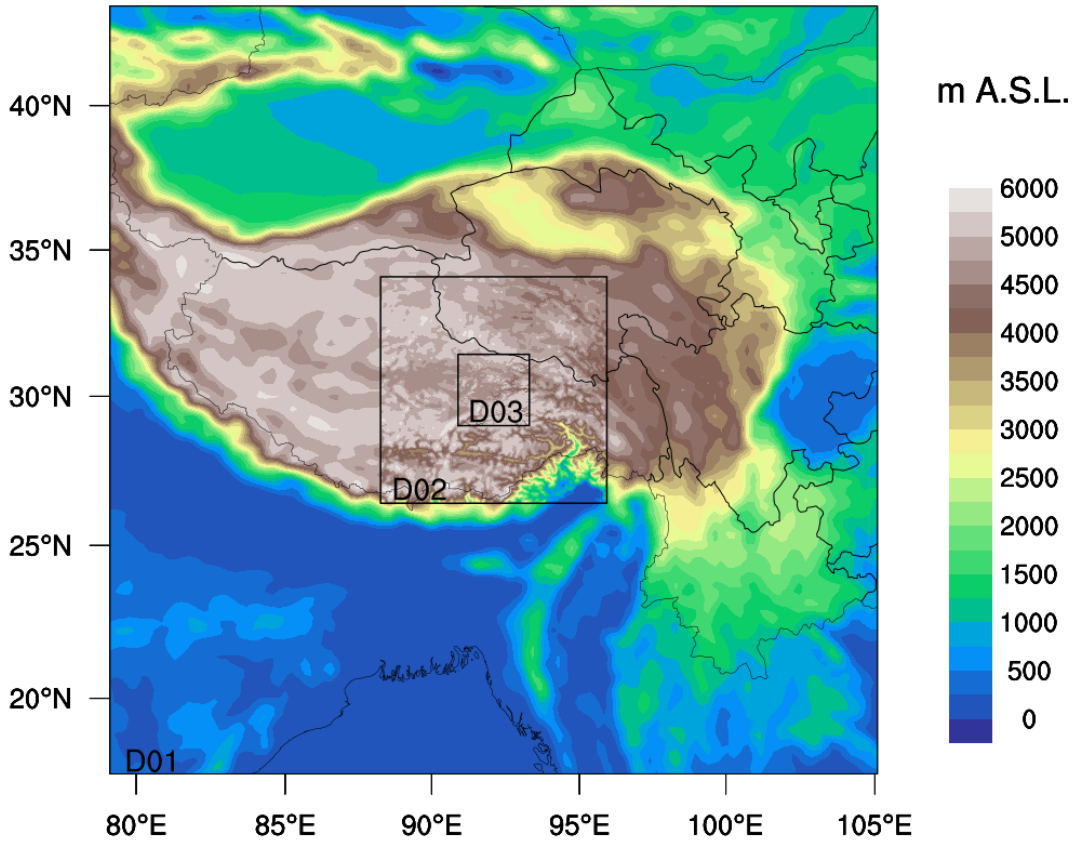

1177

1178 Figure 1. Geographic locations of the three domains used in the numerical simulation.

1179 The color bar represents the height (m) above the sea level.

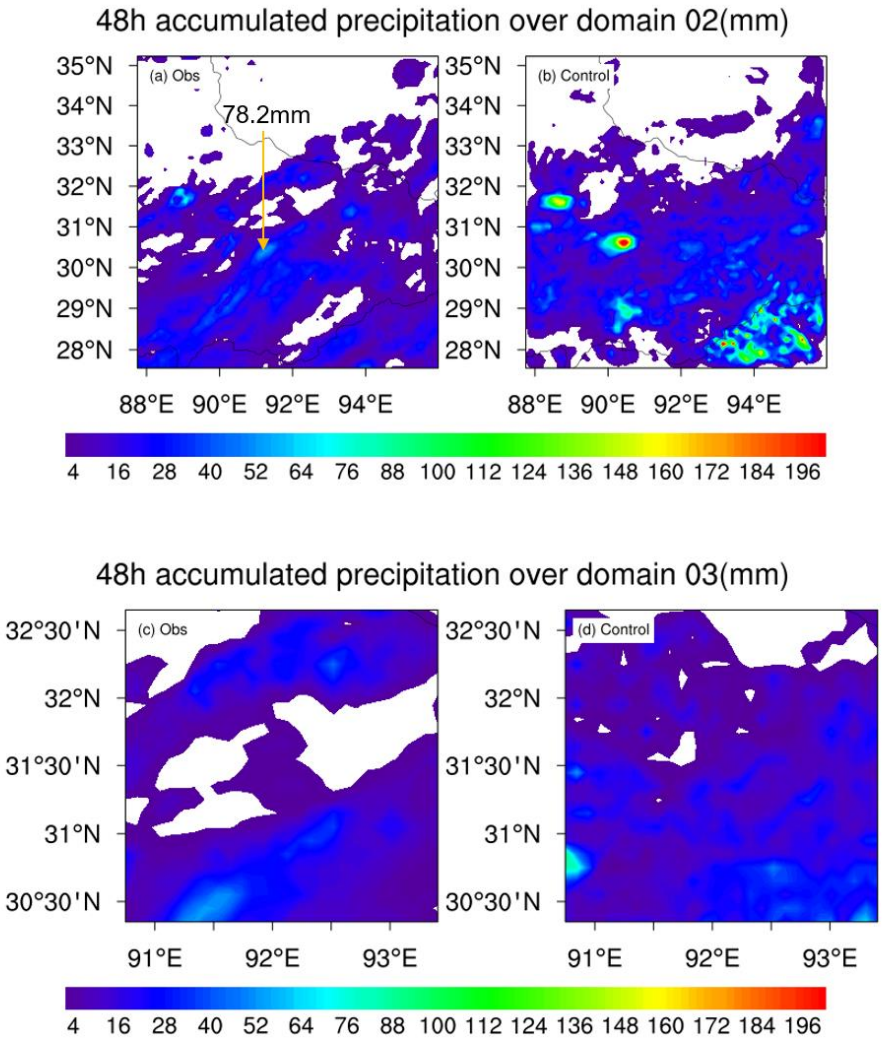

1180

1181 Figure 2. Spatial distributions of 48 h accumulated precipitation (mm) from 0000 UTC

1182 22 July to 0000 UTC 24 July 2014 in the observations and the control run over domain

1183 02 (a, b) and domain 03 (c, d).

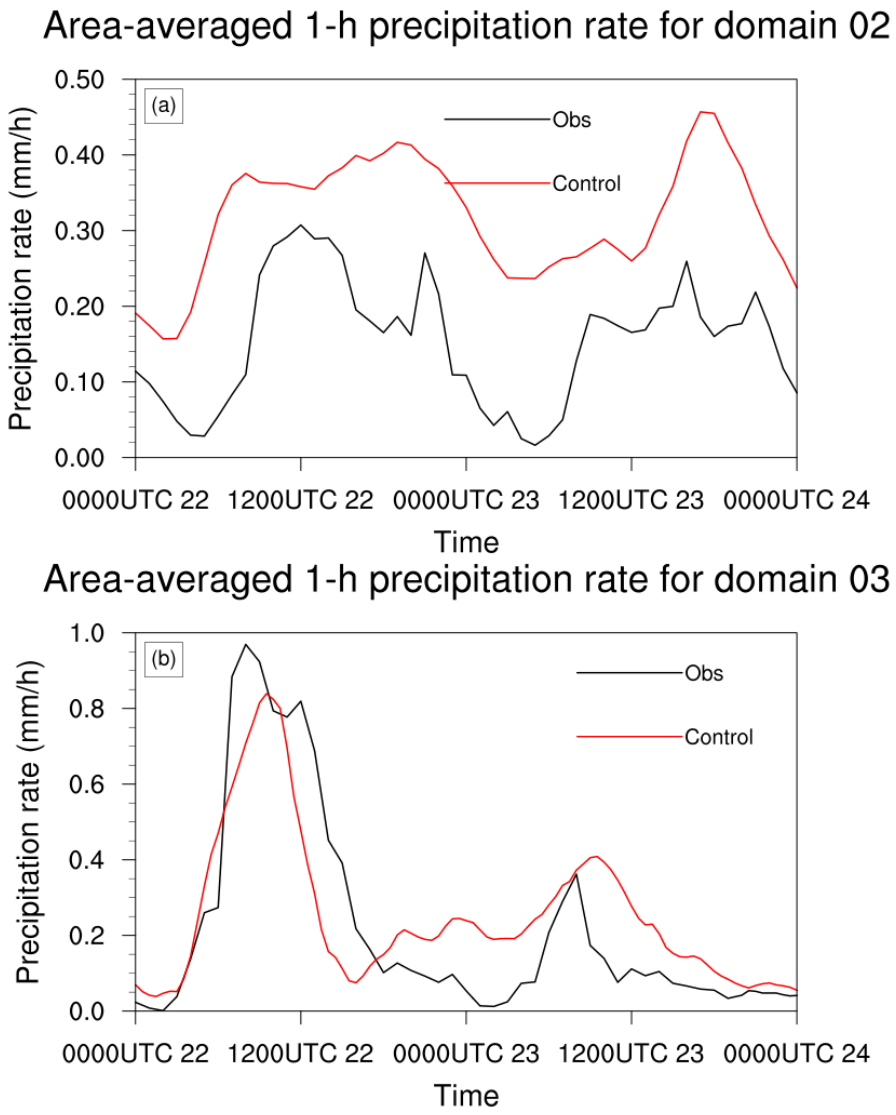

1184

1185 Figure 3. Time series of area-averaged hourly precipitation rate (mm/h) from 0000 UTC

1186 22 July to 0000 UTC 24 July 2014 over (a) domain 02 and (b) domain 03 in the

1187 observations and the control run.

1188

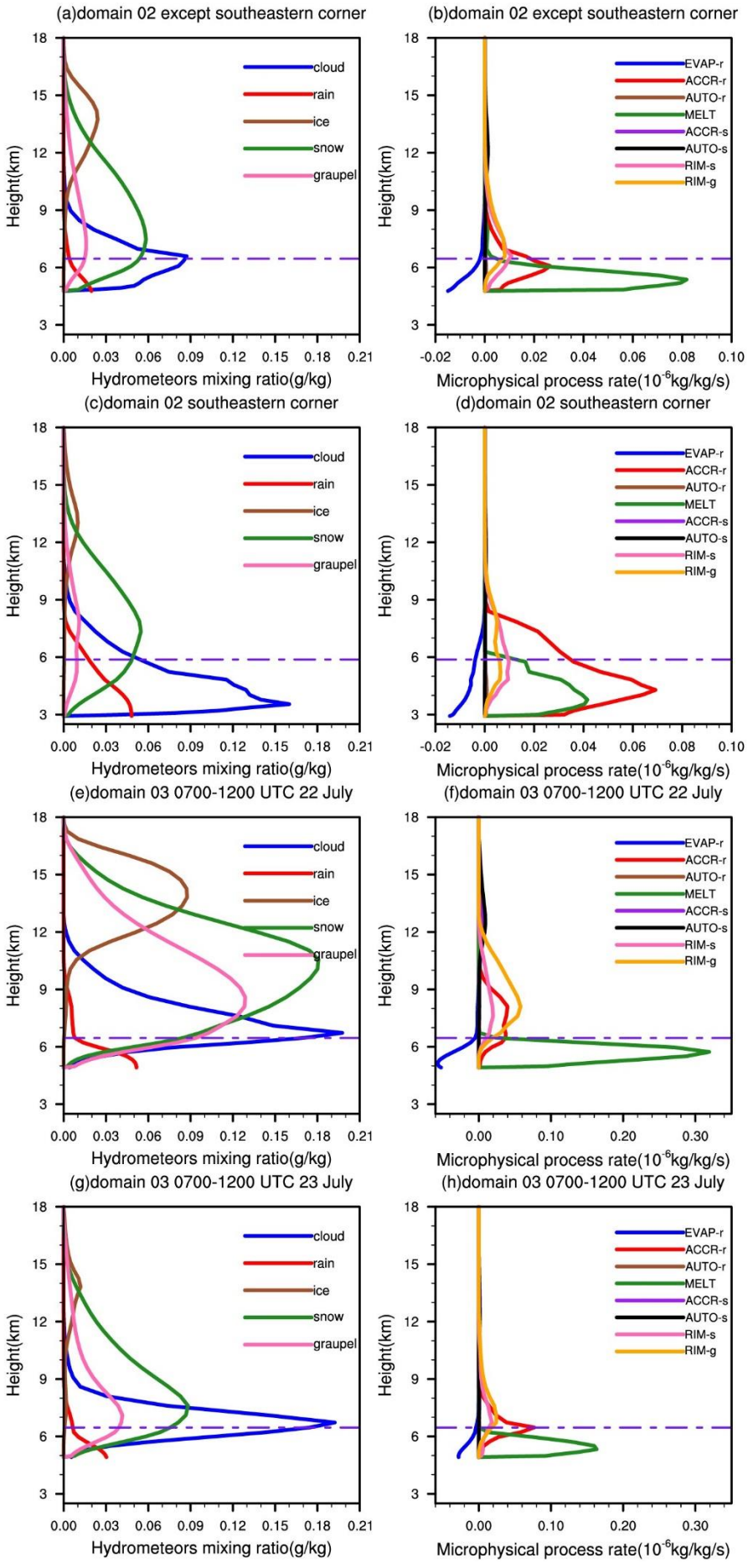
(a)domain 02 except southeastern corner
(b)domain 02 except southeastern corner
Height(km)
cloud
rain
ice
snow
graupel
EVAP-r
ACCR-r
AUTO-r
MELT
ACCR-s
AUTO-s
RIM-s
RIM-g
Hydrometeors mixing ratio(g/kg)
Microphysical process rate(10-6kg/kg/s)
(c)domain 02 southeastern corner
(d)domain 02 southeastern corner
(e)domain 03 0700-1200 UTC 22 July
(f)domain 03 0700-1200 UTC 22 July
(g)domain 03 0700-1200 UTC 23 July
(h)domain 03 0700-1200 UTC 23 July

1189

Figure 4. Mean vertical profiles of mixing ratios (g/kg) of cloud droplets (q_c), raindrops (q_r), ice particles (q_i), snow particles (q_s), graupel particles (q_g) and their primary microphysical processes in the control run (a, b) averaged for 48 h over domain 02 except southeastern corner, (c, d) averaged for 48 h at the southeastern corner over domain 02, averaged during two precipitation peaks (e, f) 0700-1200 UTC 22 July 2014 and (g, h) 0700-1200 UTC 23 July 2014 over domain 03. The purple dot-dash lines denote the heights of 0 ℃ isotherm. The meanings of the symbols in the legends are shown in Appendix A.

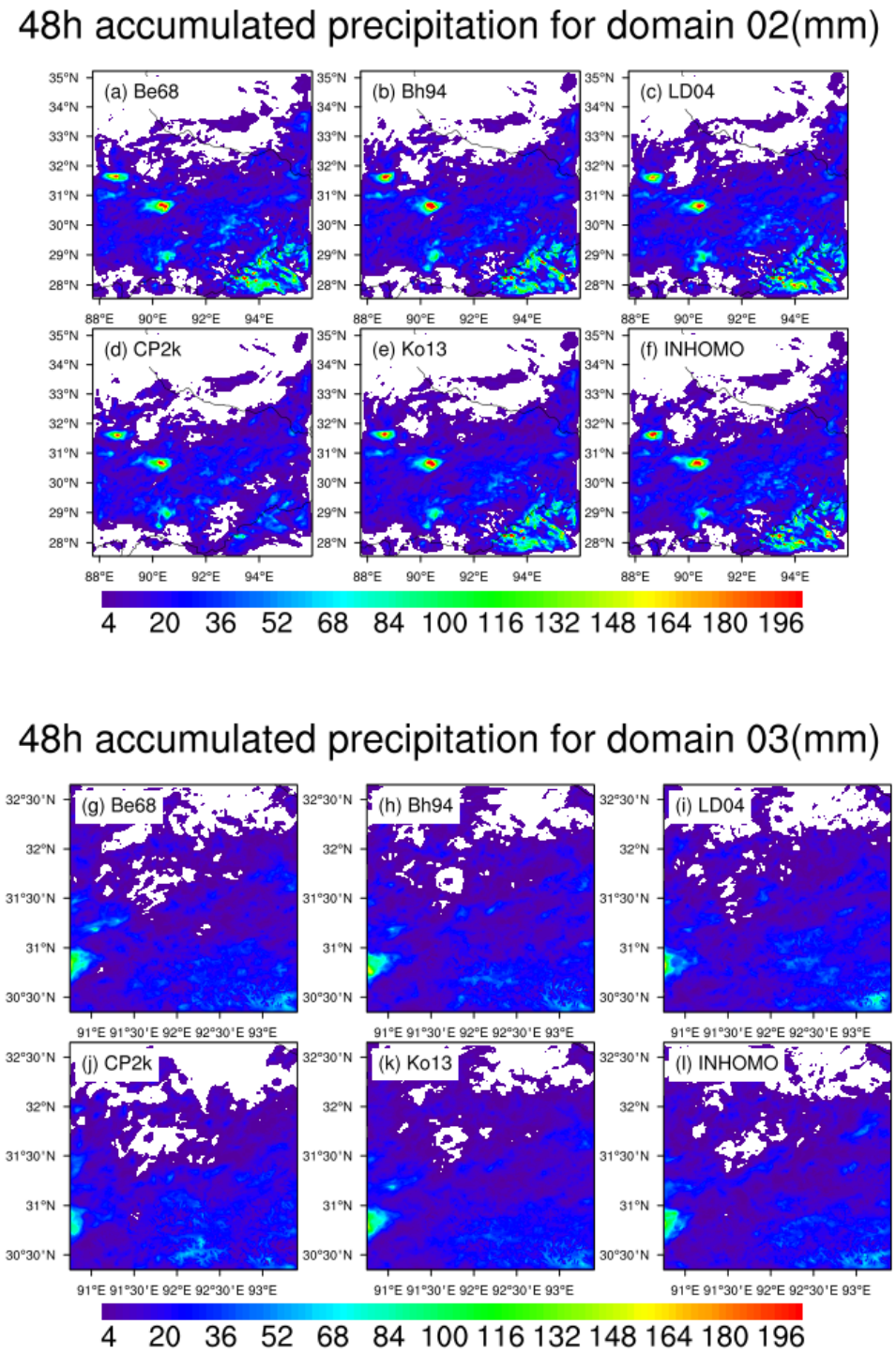

1199

1200 Figure 5. Spatial distributions of 48 h accumulated precipitation (mm) during 0000

1201 UTC 22 July to 0000 UTC 24 July 2014 from observations and all sensitivity

1202 simulations over (a-f) domain 02 and domain 03.

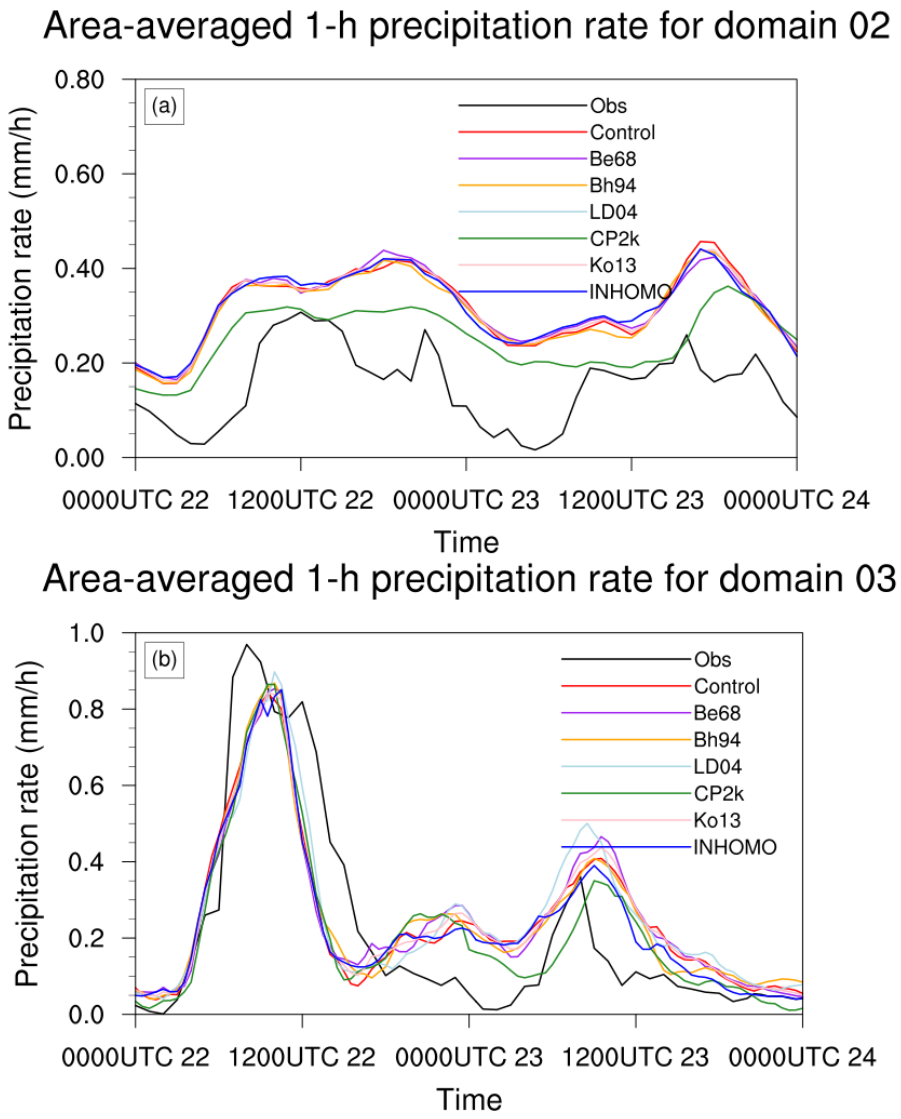

1203

1204 Figure 6. Time series of area-averaged hourly precipitation rate (mm/h) from 0000 UTC

1205 22 July to 0000 UTC 24 July 2014 over (a) domain 02 and (b) domain 03 from the

1206 observations and all simulations.

1207

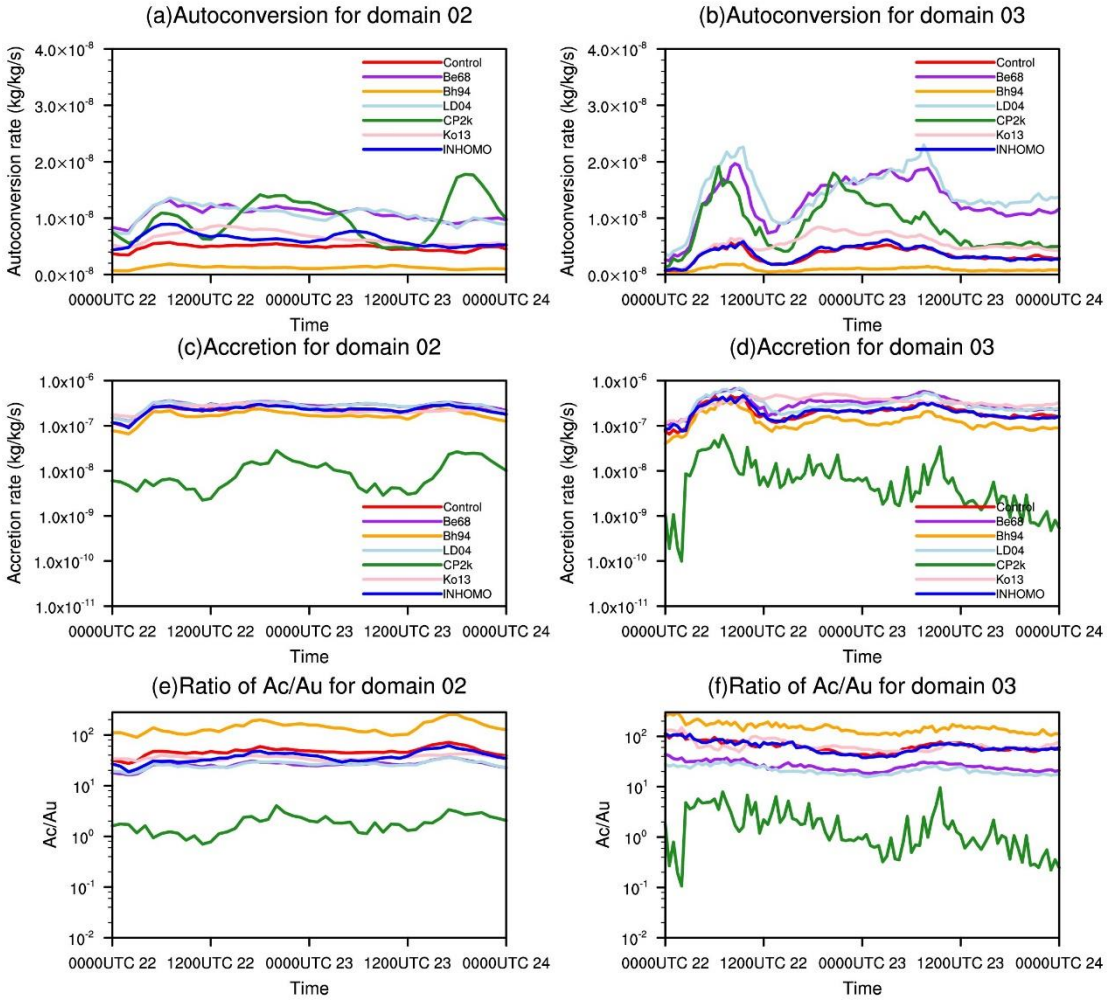

1208

1209 Figure 7. The time series of area-averaged autoconversion rate, accretion rate, and the

1210 ratio of accretion rate to autoconversion rate (A_c/A_u) over (a, c, e) domain 02 and (b, d,

1211 f) domain 03 for all simulations, respectively.

1212

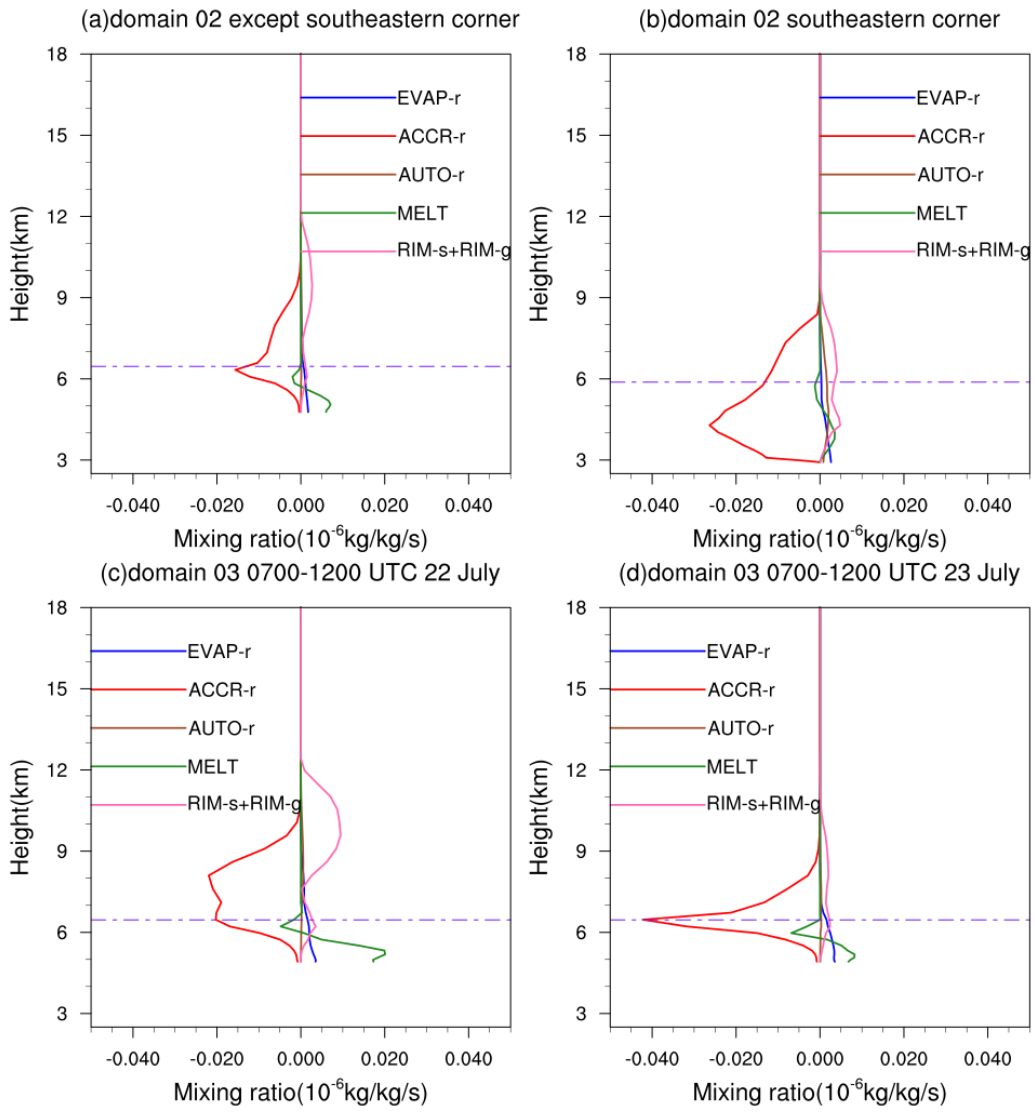

1213

1214 Figure 8. Differences of mean vertical profiles of the dominated microphysical

1215 processes conversion rates between CP2k and the control run (CP2k-Control) from (a)

1216 domain 02 except the southeastern corner, (b) the southeastern corner of domain 02,

1217 and during the two precipitation peak periods (c) 0700-1200 UTC 22 July and (d) 0700-

1218 1200 UTC 23 July over domain 03. The purple dot-dash lines denote the heights of 0 ℃

1219 isotherm. The meanings of the symbols in the legends are shown in Appendix A.

1220

1221

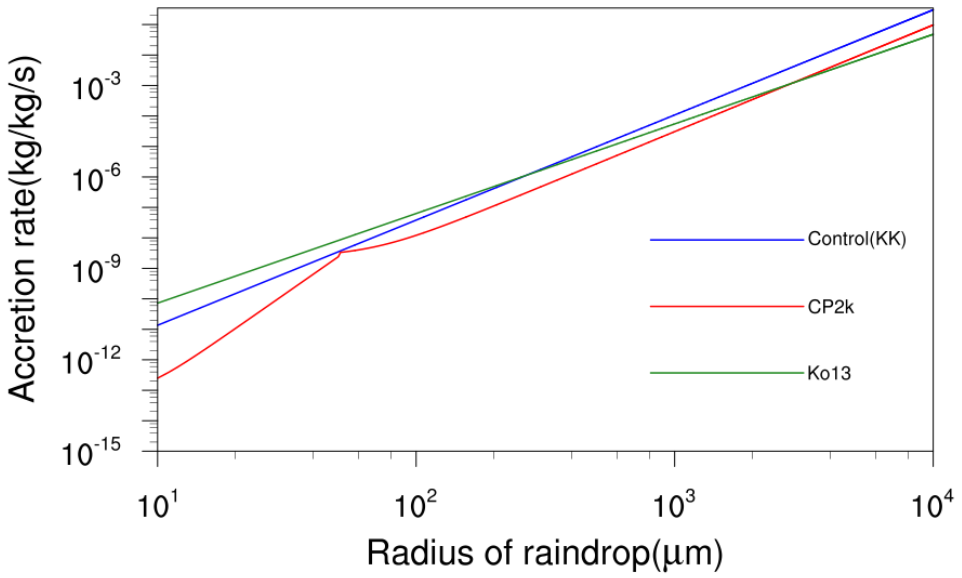

1222

1223 Figure 9. The accretion rate as a function of raindrop radius with fixed cloud mixing

1224 ratio q_c = 1 g/kg, the radius of cloud droplet R_c = 10 μm, number concentration of

1225 raindrops N_r = 4000 /m^3 for the three accretion schemes.

1226

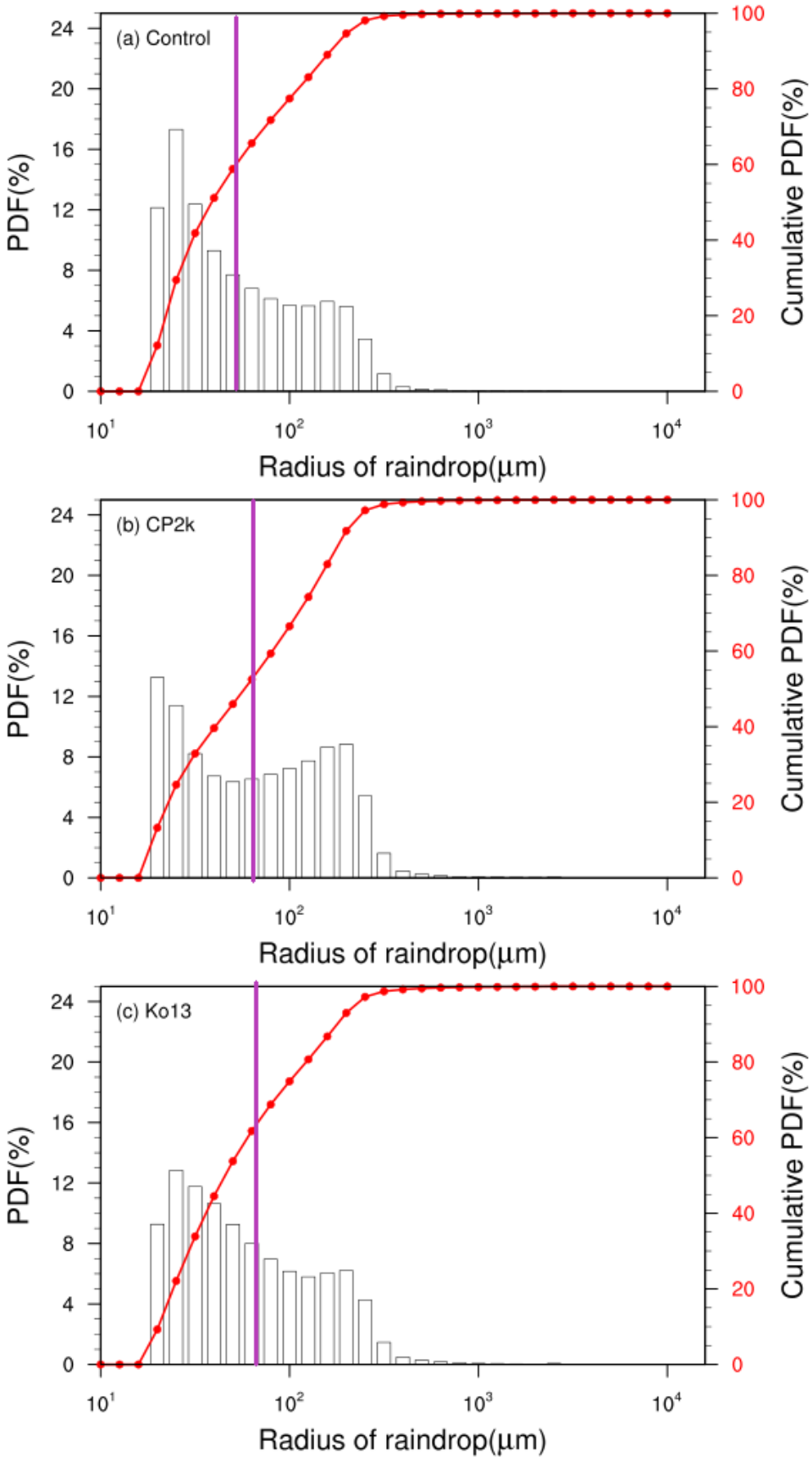

1227

1228 Figure 10. Probability distribution function (PDF) and cumulative PDF of raindrop

1229 radius involved in the accretion process for (a) the control run, (b) CP2k, and (c) Ko13.

1230 The purple line denotes the radius of raindrop equal to 50 μm.

1231

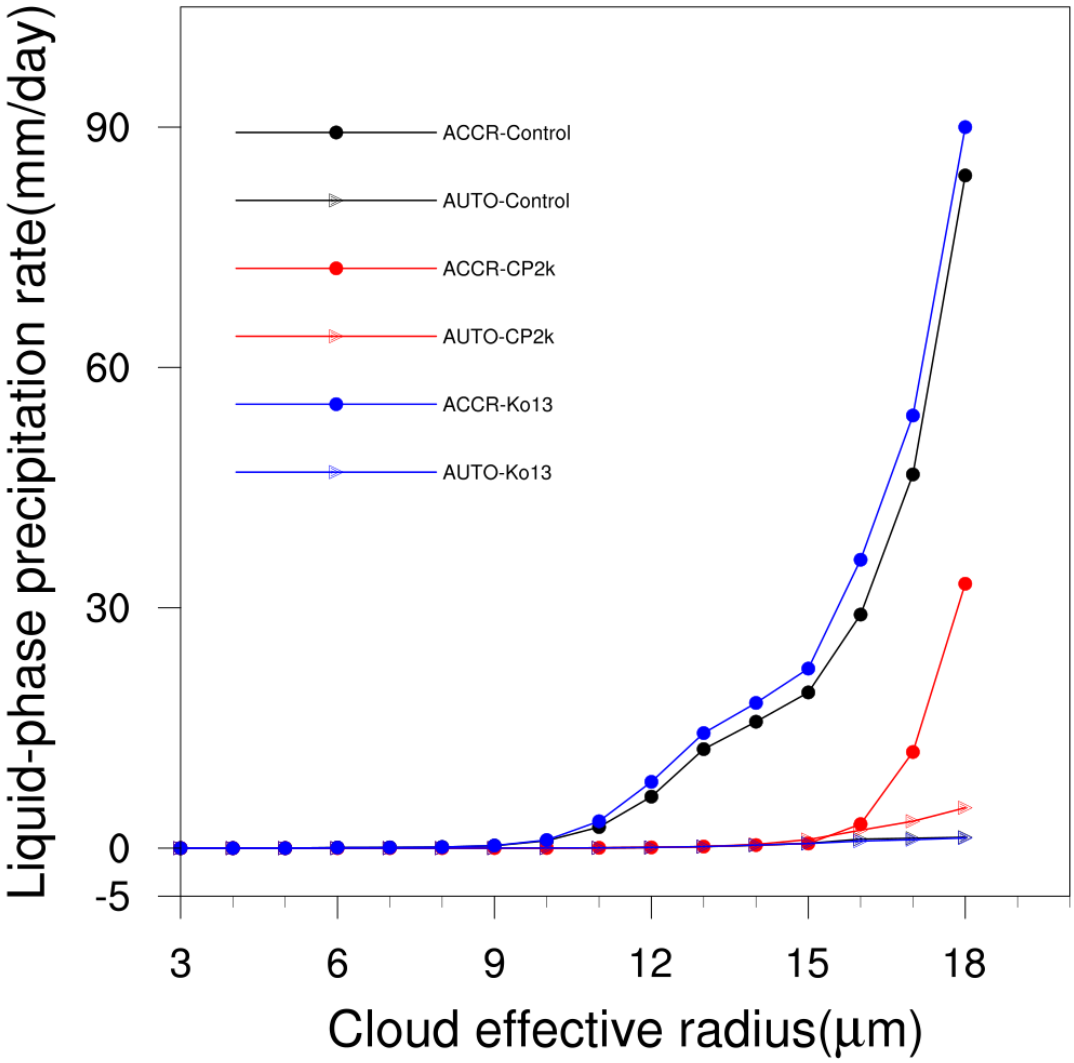

1232

1233 Figure 11. Dependence of liquid-phase precipitation intensity on cloud effective radius

1234 from the three accretion schemes during 0000 UTC 22 July to 0000 UTC 24 July 2014

1235 over domain 03.

1236

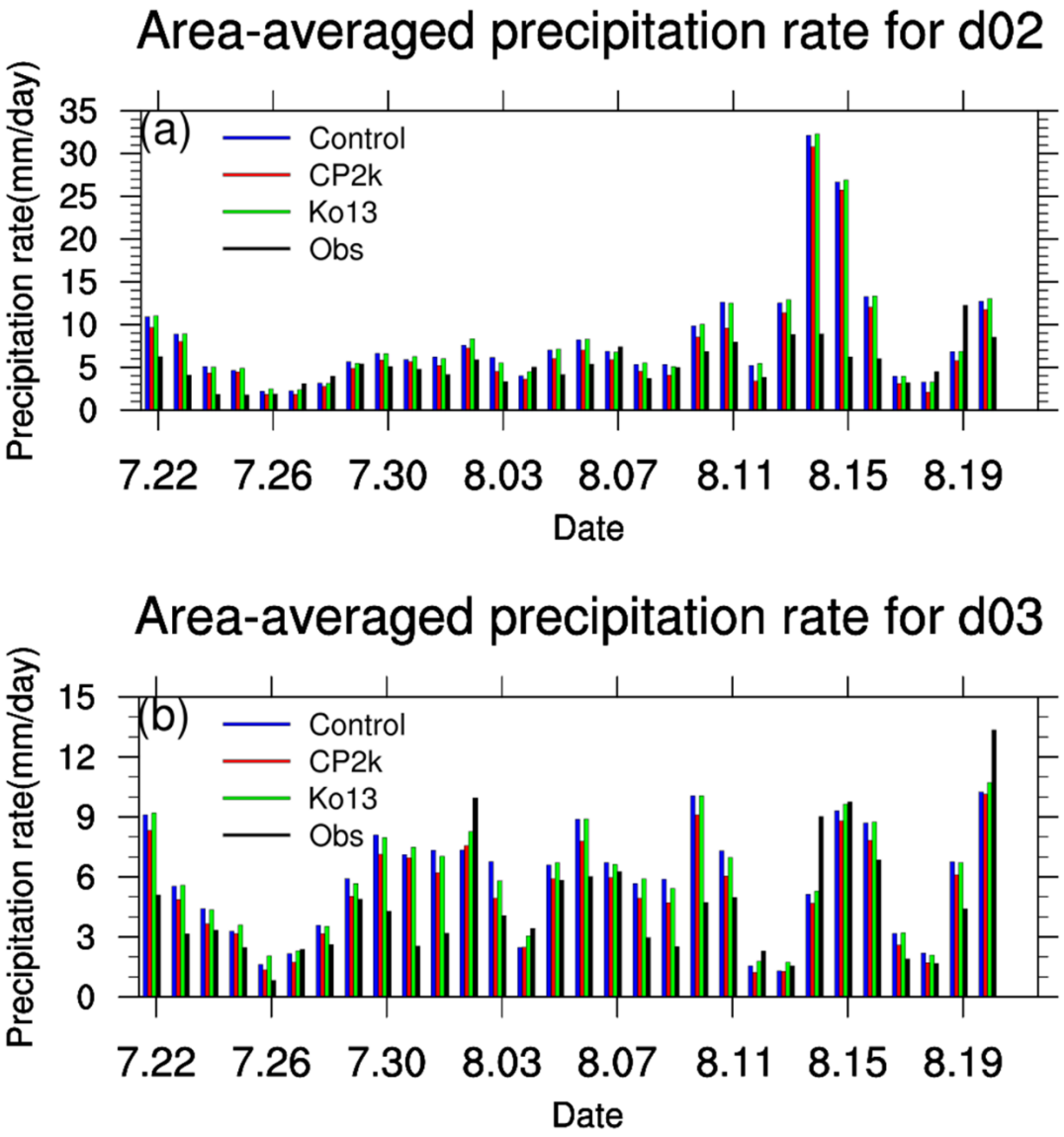

1237

1238 Figure 12. Time series of area-averaged daily precipitation rate (mm/day) from 0000

1239 UTC 22 July to 0000 UTC 20 August 2014 over (a) domain 02 and (b) domain 03 in

1240 the observations and three accretion cases (the control run, CP2k and Ko13).

1241

1242

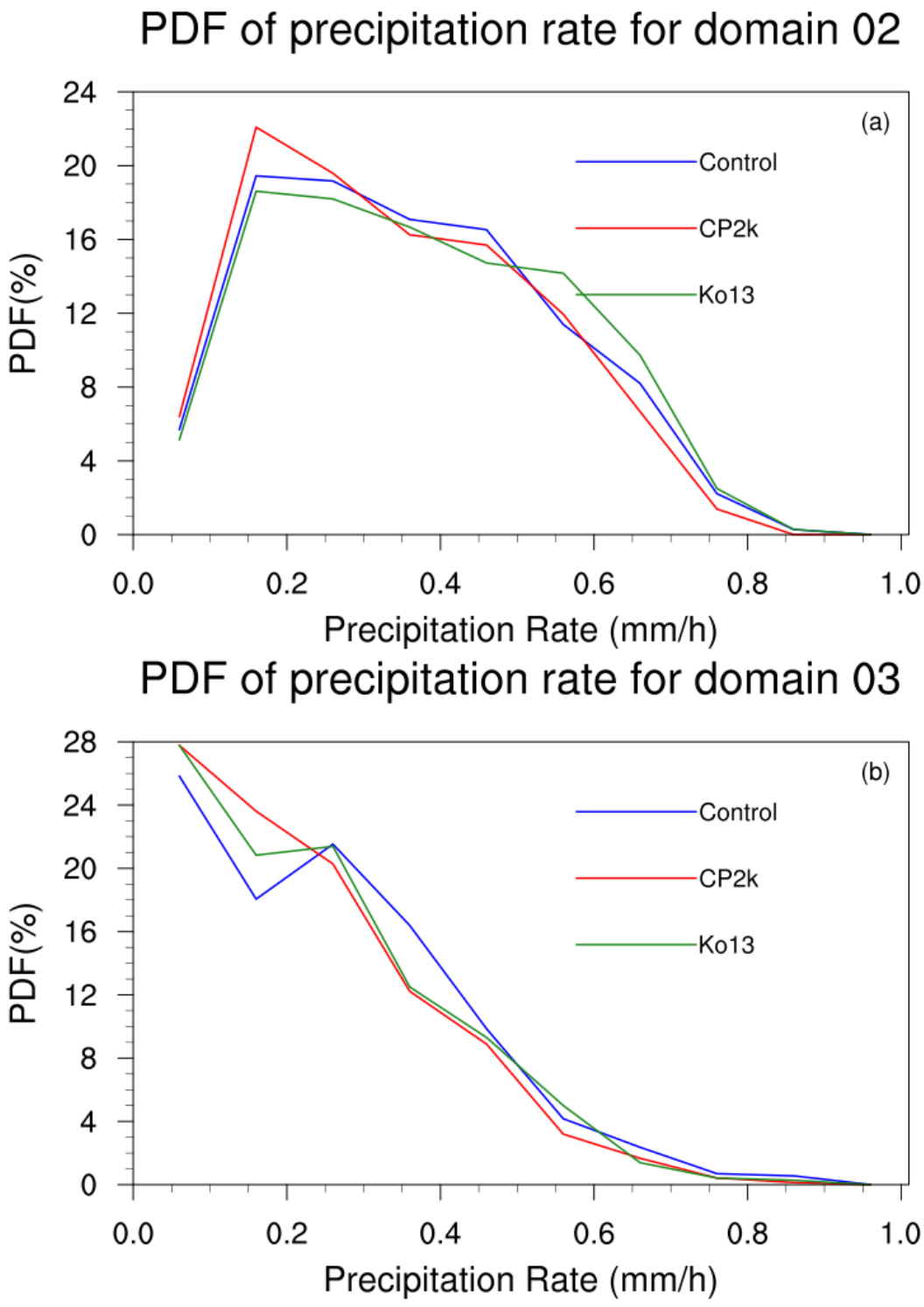

1243

1244 Figure 13. Probability distribution function (PDF) of precipitation rate (mm/h) from

1245 0000 UTC 21 July to 0000 UTC 21 August 2014 over (a) domain 02 and (b) domain 03

1246 in the three accretion cases (the control run, CP2k and Ko13).

1247